ULTRASOUND-MODULATED OPTICAL TOMOGRAPHY FOR BIOMEDICAL APPLICATIONS

A Dissertation

by

JUN LI

Submitted to the Office of Graduate Studies of
Texas A&M University
in partial fulfillment of the requirements for the degree of

DOCTOR OF PHILOSOPHY

August 2004

Major Subject: Biomedical Engineering

ULTRASOUND-MODULATED OPTICAL TOMOGRAPHY FOR BIOMEDICAL APPLICATIONS

A Dissertation

by

JUN LI

Submitted to the Office of Graduate Studies of
Texas A&M University
in partial fulfillment of the requirements for the degree of

DOCTOR OF PHILOSOPHY

Approved as to style and content by:

Lihong V. Wang (Chair of Committee)	Ohannes Eknoyan (Member)
Gerard L. Coté (Member)	Jay D. Humphrey (Member)
William Hyman (Head of Department)	

August 2004

Major Subject: Biomedical Engineering

ABSTRACT

Ultrasound-modulated Optical Tomography for Biomedical Applications.

(August 2004)

Jun Li, B.Eng., Huazhong University of Science and Technology;
M.Eng., Huazhong University of Science and Technology;
Ph.D., Huazhong University of Science and Technology
Chair of Advisory Committee: Dr. Lihong V. Wang

I experimentally studied ultrasound-modulated optical tomography, which holds the promise for biomedical diagnosis. I measured the degree of polarization of laser speckles generated by scattered light transmitted through turbid media, investigated three signal-detection schemes for extracting the intensity of the ultrasound-modulated light, carried out experiments to image thick biological-tissue samples, and studied two techniques providing resolution in the cross-sections containing the ultrasonic axis.

The study of degree of polarization presented results important for the understanding of polarization phenomena in turbid media. I explored an optical-filtering based signal detection scheme, improved the parallel-lock-in speckle detection scheme and proposed a speckle-contrast detection scheme. With the speckle-contrast detection scheme, I successfully obtained images of biological-tissue samples up to 50 mm thick. Further I studied frequency-swept ultrasound-modulated optical tomography for sub-millimeter resolution imaging, and developed ultrasound-modulated optical computed tomography that was based on a back-projection image reconstruction method and obtained clear images of biological-tissue samples.

DEDICATION

This work is dedicated to

my wife Zhen Tan,

my son Erik,

my parents and my sister,

for their understanding and support.

ACKNOWLEDGEMENTS

I am greatly indebted, and wish to express my sincere gratitude to my advisor, Dr. Lihong V. Wang, for his invaluable advice, continuous guidance and encouragement in the accomplishment of this dissertation. I want to thank him for the many thought-provoking discussions we have had, the detailed comments and suggestions on my research, and the numerous time he spent with me.

I would like to thank my committee members, Dr. Jay D. Humphrey, Dr. Gerard L. Coté, and Dr. Ohannes Eknoyan, for their helpful advice on this dissertation.

I am grateful to all the colleagues working with the Optical Imaging Laboratory at Texas A&M University. I would like to especially thank Sava Sakadžić, Geng Ku, Xiao Xu, Konstantin Maslov, Yuan Xu, Minghua Xu, and Xueding Wang for the helpful discussions we had and the assistance they gave me in my experiments. Thanks also go to alumni, Gang Yao, Hui Li, and Dazi Feng. Their help is greatly appreciated.

Finally, I would like to thank my family for their constant encouragement and support through my four-year study.

TABLE OF CONTENTS

LIST OF FIGURES

FIGURE Page

FIGURE Page

FIGURE Page

FIGURE Page

CHAPTER I

INTRODUCTION

1. Biomedical optical imaging

Optical imaging is attractive in the biomedical field because it is a non-invasive, non-ionizing, and functional imaging modality.[1] Compared with X-ray imaging which uses ionizing radiation (e.g., ~50 KeV photons), optical imaging is safe because it uses low-energy non-ionizing radiation: photon energy is only ~2 eV for 500-nm-wavelength radiation. It is inexpensive compared with magnetic resonance imaging (MRI). And, compared with ultrasound imaging, optical imaging provides better soft-tissue contrast, which is based on optical properties (i.e., absorption and scattering). Because the absorption and scattering of biological tissues in the visible and near infrared region are related to the molecular constituents of tissues and electronic and/or vibration structures at the molecular level, they are intrinsically sensitive indicators of tissue abnormalities and functions.[2-4] Cancerous tissues manifest significant architectural changes at the cellular and sub-cellular levels, which are revealed in the optical scattering properties.[5] Angiogenesis and hyper-metabolism, which are hallmarks of cancers, are intrinsic to the optical absorption properties.[6] Optical imaging holds promise for early cancer diagnosis. Optical information can also be used to deduce physiological parameters such as the oxygen saturation of hemoglobin. This makes optical functional imaging possible.

This dissertation follows the style and format of Applied Optics.

Oxygen saturation is closely related to the metabolic state of lesions and is an important diagnostic parameter.

However, optical imaging faces the challenge: strong optical scattering in biological tissues, which leads to poor image resolution. Because biological tissues are optically turbid media, light is strongly scattered inside tissues. A typical scattering coefficient for visible light in biological tissues is 100 cm^{-1}, compared to 0.2 cm^{-1} for X-ray used in medical diagnosis. Scattering causes light to change its direction and multiple scattering causes light to lose its original direction. Light transmitted through tissues can be classified as: ballistic light, quasi-ballistic light and diffuse light. Ballistic light experiences no scattering and carries direct imaging information. Quasi-ballistic light experiences minimal scattering and carries some imaging information. Diffuse light follows tortuous paths and carries little direct imaging information. Correspondingly, optical imaging techniques are classified as: ballistic imaging and diffuse imaging. In the ballistic imaging, diffuse light is rejected and ballistic or quasi-ballistic light is collected. The imaging is suitable for thin tissue samples but suffers loss of signal and resolution for thick tissues because of the strong scattering of light by the tissue. The time-gated optical imaging[7-9] and optical coherence tomography[10,11] belong to the ballistic imaging. The diffuse imaging is developed for thick-tissue samples, which includes frequency domain optical imaging[12] and DC diffuse tomography.[13] In this kind of imaging, sophisticated image reconstruction algorithms based on diffuse equation or transport equation are applied. The image quality however is usually algorithm dependent and the image resolution is not good enough.

2. Ultrasound-modulated optical tomography (UMOT)

To overcome the problem of poor image resolution in imaging of thick tissues (over several millimeters), hybrid techniques that combine optical and ultrasonic techniques have been explored. These methods include photoacoustic imaging,[14-16] sonoluminescent tomography,[17] and ultrasound-modulated optical tomography. Because ultrasonic waves are scattered less in biological tissues than light waves, they can be used to provide spatial information directly for imaging. Present study is focused on ultrasound-modulated optical tomography. In UMOT, an ultrasonic wave is focused into biological tissues to modulate the light passing through the ultrasonic zone. The modulated (or tagged) light carries the ultrasonic frequency and, therefore, can be discriminated from the background un-modulated light, and its origins can be derived from the position of the ultrasonic column inside the tissue. The advantage of ultrasound-modulated optical tomography is that the technique combines optical contrast with ultrasonic resolution.

Three possible mechanisms are involved in the ultrasonic modulation of light in turbid media. The first mechanism is based on ultrasound-induced variations of the optical properties of the media. When an ultrasonic wave propagates in a scattering medium, the medium is compressed and rarified by the ultrasonic wave. Variations of density cause the variations of optical properties of the medium, i.e., optical absorption coefficient, scattering coefficient, and the index of refraction. In consequence, the detected intensity of light varies with the ultrasonic wave. This mechanism, which was studied recently by Mahan *et al.*,[18] does not require the use of a coherent light source. However, ultrasonic modulation of incoherent light has not been experimentally observed because it is too weak. The second mechanism is based on variations of the optical phase in response to ultrasound-induced displacements of scatterers. The displacements of scatterers, which follow ultrasonic amplitudes, modulate the path lengths of light traversing through the ultrasonic field. Multiply scattered light accumulates modulated physical path lengths along its path. Consequently, the intensity of the speckles formed by the multiply scattered light fluctuates with the ultrasonic wave. A theory developed by Leutz and Maret[19] modeled this mechanism but is valid only when the scattering mean free path is much greater than the acoustic wavelength. The third mechanism is based on variations of the optical phase in response to ultrasonic modulation of the index of refraction. As a result of ultrasonic modulation of the index of refraction, the optical phase between two consecutive scattering events is modulated. As in the second mechanism, multiply scattered light accumulates modulated phases along its path, and the modulated phase causes the intensity of the speckles formed by the multiply scattered light to vary with the ultrasonic wave. Both the second and the third mechanism require the use of coherent light. Recently, Wang[20,21] and Sakadžić[22] developed comprehensive analytic and Monte Carlo models based on both of the mechanisms for the ultrasonic modulation of coherent light in scattering media.

UMOT has been studied experimentally by several research groups. Marks *et al.*[23] investigated the combination of pulsed ultrasound and laser light and detected an ultrasound-modulated optical signal in a homogeneous turbid medium. Wang *et al.*[24,25] developed UMOT with continuous-wave ultrasound and obtained images in tissue-simulating turbid media. The signal-to-noise ratio (SNR) was improved significantly compared with the pulsed ultrasound modulation. Two-dimensional (2D) images were obtained in their experiment. Kempe *et al.*[26] studied UMOT in tissue phantoms. They obtained the modulated signal in a dense latex sphere solution and obtained images of absorbent objects in a tissue phantom. In these experiments, a single detector, e.g., a photomultiplier or a photodiode, was used. The detection area usually was much larger than a single speckle size and multiple speckles were detected, which were accumulated to yield the signal. The detected modulation depth was small because it was decreased by the square root of the number of speckles.

A parallel speckle detection was developed by Leveque *et al.*,[27] in which a CCD camera was employed and a source-synchronized lock-in detection was applied. The CCD camera played as multiple detectors: each pixel acted as a single detector which detected a single speckle. Averaging signals over the pixels greatly increased the signal-to-noise ratio. They obtained one-dimensional (1D) images of biological tissue. Yao *et al.*[28] subsequently obtained 2D images of multiple objects buried in biological tissues by use of parallel speckle detection. Li *et al.*[29] developed multiple methods to improve the parallel speckle detection: reduce the acquisition time and improve the signal-to-noise ratio. Selb. *et al.*[30] explored non-linear effects in imaging. Recently, Li *et al.*[31] developed speckle-contrast detection for tomography and obtained images of biological-tissue samples up to 50 mm thick.[32] Leveque[33] obtained three-dimensional images in biological tissues by using parallel speckle detection and scanning the ultrasonic beam in three dimensions.

To improve the spatial resolution along the ultrasonic axis, Wang and Ku[34] developed a frequency-swept technique, in which the ultrasonic frequency is a function of the spatial position along the ultrasonic axis. The ultrasound-modulated optical signal generated at different positions along the ultrasonic axis can be resolved in frequency domain by

Fourier transform. Yao *et al.*[35] further developed the technique by combining it with the parallel detection and obtained 2D images of biological tissues in which one dimension was along the ultrasonic axis. They demonstrated the scalability of the spatial resolution along the ultrasonic axis by adjusting the parameters of the frequency-swept ultrasound. Forget *et al.*[36] recently developed the technique by combining the above two techniques: a film sequence of optical signals was recorded with a CCD camera that played as multiple detectors, and Fourier transforms were taken on the signals. Pulsed ultrasound was also studied to provide spatial resolution along the ultrasonic axis.[37,38] More recently, Li *et al.* [39] developed a technique called ultrasound-modulated optical computed tomography and obtained images of cross-sections containing the ultrasonic axis.

Besides the imaging in transmission configurations, imaging in side-detection and reflection-detection configurations has also been studied. Li *et al.*[32] studied a side-detection configuration in thick tissue imaging and did comparison with transmission-detection configuration. Lev *et al.*[40,41] obtained a 1D image of an absorbent object and measured optical properties in a reflection configuration. Leveque *et al.*[42] obtained an image of a tissue-phantom object buried in a biological tissue sample in a reflection configuration.

Because it has the advantage of combining optical contrast with ultrasonic resolution, UMOT holds the promise for broad applications in biomedical diagnosis, e.g, breast cancer diagnosis, skin cancer diagnosis, ect.. Since it is a new technology in the field, investigations are needed for understanding and developing the technology. There will be challenges to be overcome during its development towards practical applications. For example, in practice, the sample thickness in breast cancer diagnosis will be 5-10 cm.

This requires UMOT to be able to image thick tissue samples. Signal detection will be an important issue. Development of signal detection techniques is expected. In addition, the detection configuration should be developed to meet the requirement of convenience for practical applications.

The work I present here focuses on investigating signal-detection techniques and imaging methods for UMOT. In Chapter II, polarization properties of speckle fields generated by scattered light transmitted through turbid media was studied. Multiple signal-detection schemes were investigated experimentally in Chapter III. In Chapter IV, experiments were conducted to image thick biological tissues by use of speckle-contrast detection and two kinds of detection configurations were studied. In Chapter V, two techniques for obtaining images of cross-section containing ultrasonic axis were studied, with which three-dimensional images are obtainable. Finally, a conclusion was given in Chapter VI.

CHAPTER II

DEGREE OF POLARIZATION IN LASER SPECKLES GENERATED FROM TURBID MEDIA[*]

1. Introduction

Polarization is a unique contrast mechanism in biomedical optical imaging.[43 – 45] Polarization techniques have been employed to reject[46] or accept[47] multiply scattered light from turbid media. In this chapter I studied degree of polarization in laser speckle fields generated from scattered light transmitted through turbid media. The study is not only helpful to understanding the polarization phenomenon of laser speckles but also helpful to guiding the applications of polarization in our optical imaging as well as in the field of biomedical optics.

There have been a number of publications on transmission of polarized light through a scattering medium. Sankaran *et al.*[48] experimentally studied the degree of polarization (DOP) of scattered light from biological tissues and tissue phantoms. Because a coherent-light source was generally used in these experiments, speckle patterns played significant roles in the polarization measurements. The statistics of laser speckle patterns, including partially polarized speckle patterns, was well described in Goodman's chapter.[49] In fact, partially polarized speckle patterns have been studied extensively in recent years.[50-53] Fercher and Steeger[50,51] determined the theoretical first-order statistics of Stokes parameters and later verified the theory with experiments. Brosseau *et al.*[53] studied the

---

[*] Reprinted with permission from J. Li, G. Yao, and L.-H. V. Wang, "Degree of polarization in laser speckles from turbid media: Implications in tissue optics," J. Biomed. Opt. **7**, 307–312 (2002). Copyright 2002 International Society for Optical Engineering.

statistics of normalized Stokes parameters and discussed potential applications. Freund *et al.*[54] proposed microstatistics to describe the polarization behavior of a single coherence area in a speckle field. The work was focused on deriving polarization correlation functions for extracting information about the direction of the incident polarization from the speckle pattern. Tarhan *et al.*[55] further investigated the microstatistics; they measured the intensity at many points in a speckle pattern for a given polarization angle of the incoming laser beam and obtained the probability density distributions for the parameters in the statistics. However, these two studies did not evaluate the DOP at those points in the speckle field, which is a key parameter for the understanding of polarized speckle fields. Elies *et al.*,[56] in a more recent investigation on speckle polarization, observed the speckle field produced by light reflected from a polished aluminum sample with a CCD camera. Their results showed that depolarization among multiple speckle grains increased with sample inclination although each speckle grain remained polarized.

Here I investigated the polarization in a speckle field formed by coherent light being transmitted through a surface-scattering medium (a ground-glass plate) or a volume-scattering medium (a wax plate).[57] The degree of polarization was measured both within a single coherence area and over multiple coherence areas and was further modeled theoretically. Although it is widely acknowledged that multiple scattering events in volume-scattering media can depolarize polarized incident light and hence reduce the DOP, my study demonstrated that the measured DOP depended significantly on the conditions of observation.

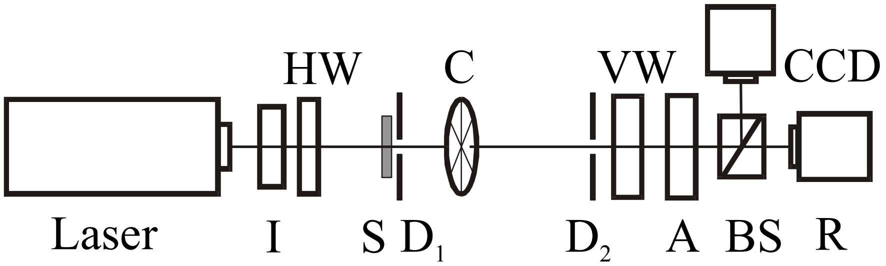

Fig. 1. Experimental setup. I, optical isolator; HW, half-wave plate; S, sample; D_1 and D_2, irises; C, chopper; VW, variable-wave plate; A, analyzer; BS, non-polarizing beam splitter; R, photoreceiver.

2. Experiments and simulation

The experimental setup is shown in Fig. 1. A diode laser (SDL, TC40, 850 nm) emitted a beam of 1.5 mm in FWHM diameter and of 60 m in coherence length. After passing through an optical isolator and a half-wave retardation plate, the beam was horizontally linearly polarized with a DOP of 0.99 and an intensity fluctuation of ~1%, where the isolator and the retardation plate were used to prevent back reflection into the laser and to fine-tune the orientation of the polarization, respectively. The beam was incident upon the sample to produce a speckle field by the transmitted light. An iris was set closely behind the sample to control the average size of coherence areas in the speckle field. Another iris was used to select a portion of the speckle field for observation. The selected light, after passing through a variable-wave plate, a Glan-Thompson analyzer, and a non-polarizing beam splitter, was detected by a large-area photoreceiver. The variable-wave plate was calibrated to an accuracy of 99% before measurements. A chopper operating at 900 Hz modulated the beam intensity, and the output of the photoreceiver was measured with a lock-in amplifier (Stanford Research Systems, SR510) to improve the signal-to-noise ratio. The chopper was set behind the first iris (close to the sample) to ensure that only the light emerging from the sample was modulated and detected. A CCD camera (Dalsa CA-D1-0256T, 256×256 pixels) was used to monitor the speckle pattern simultaneously. A 3-mm thick wax plate was used as a volume-scattering sample, which multiply scattered the transmitted light. The wax sample was sufficiently thick to produce a speckle pattern of a high contrast, approaching the theoretical limit for unpolarized speckles ($1/\sqrt{2}$). For comparison, a ground-glass plate was used as a surface-scattering sample, which scattered light only on the surface by deforming the phase front.

The average diameter (d) of the coherence areas in the speckle field at the plane of detection, located at the second iris, was estimated by the following expression:[58]

$$d = \frac{2.44\lambda L}{D_1}, \tag{1}$$

where L is the distance between the two irises, D_1 is the diameter of the first iris, and λ is the optical wavelength. Eq. (1) is the definition of the diameter of the Airy disc, which represents the minimum speckle size in a speckle pattern[59] and can be used to estimate the average speckle size in a "fully developed" speckle pattern. By definition, a "fully developed" speckle pattern is completely polarized (DOP = 1). Although the speckle patterns in our experiments are not "fully developed" due to depolarization caused by multiple scattering,[60] for simplicity, I took Eq. (1) as an approximation for the average speckle size in our study. For measurements of a single coherence area (multiple coherence area), D_1 was set to 0.1 mm (2 mm), yielding an average diameter of coherence areas of 14.8 mm (0.74 mm) at the detection plane with L = 711 mm. By varying the area of detection determined by the size of the second iris (D_2), one could select the number of detected coherence areas ranging between less than one and plurality, which was monitored with the CCD camera. The Stokes vector **S**,[61] which describes a polarization state with four elements (S_0, S_1, S_2, and S_3), was measured for each area of detection by adjusting the variable-wave plate and the analyzer.

$$\mathbf{S} = \begin{bmatrix} S_0 \\ S_1 \\ S_2 \\ S_3 \end{bmatrix} = \begin{bmatrix} I_H + I_V \\ I_H - I_V \\ I_{45^o} - I_{135^o} \\ I_R - I_L \end{bmatrix}, \tag{2}$$

where I_H , I_V , I_{45^o} , I_{135^o} , I_R , and I_L are the light intensities measured with a horizontally linear analyzer, a vertically linear analyzer, a 45$^\mathrm{o}$ linear analyzer, a 135$^\mathrm{o}$ linear analyzer, a right circular analyzer, and a left circular analyzer, respectively. The DOP was then calculated by[61]

$$\mathrm{DOP} = (S_1{}^2 + S_2{}^2 + S_3{}^2)^{1/2} \big/ S_0 \, . \tag{3}$$

The degree of linear polarization (DOLP) and the degree of circular polarization (DOCP) could be obtained as well.

$$\mathrm{DOLP} = (S_1{}^2 + S_2{}^2)^{1/2} \big/ S_0 \, , \tag{4}$$

$$\mathrm{DOCP} = |S_3| \big/ S_0 \, . \tag{5}$$

The study was focused on the DOP. It was observed in the experiments that the DOLP and DOCP varied in similar ways as that of the DOP with the size of the detection area. Figure 2(a) shows the DOP measured within a single coherence area as functions of the size of the detection area. For the ground-glass sample, the DOP showed little variation associated with the size of the detection area and remained at ~0.99, which was approximately the same as that of the laser source. By contrast, for the wax sample, only the DOP of those small areas of detection was close to unity, and the DOP decreased as the area of detection was enlarged.

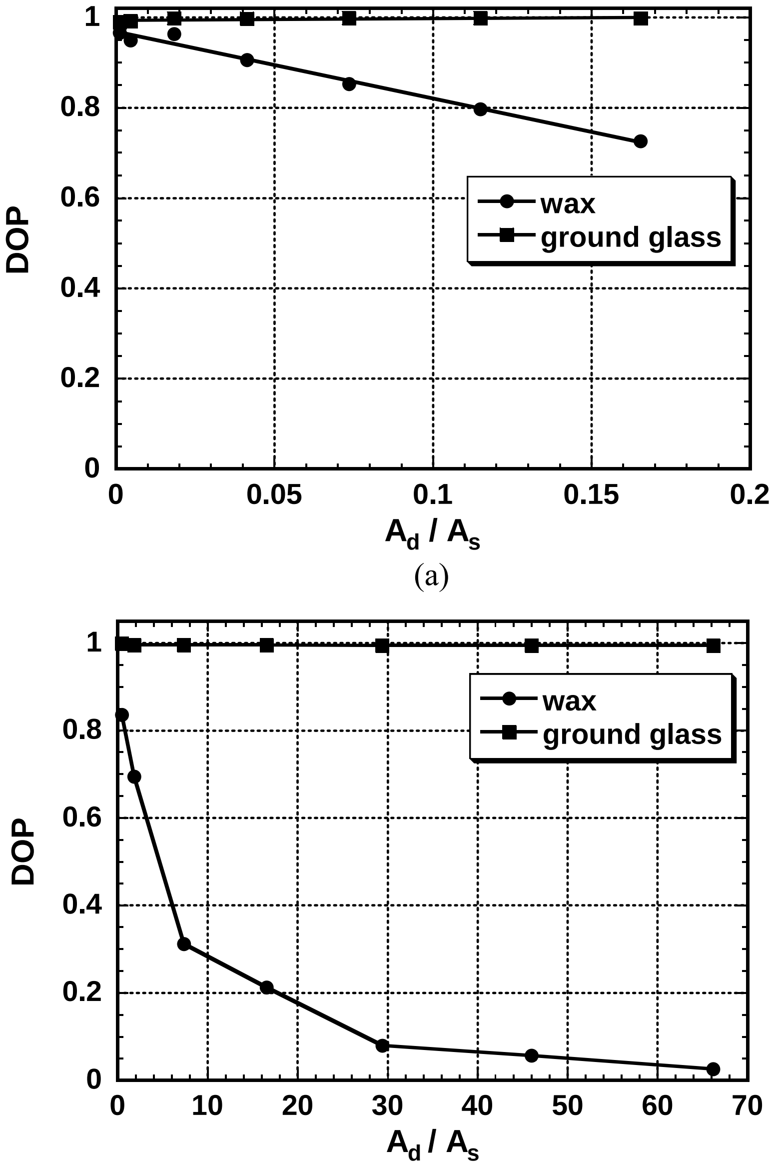

(a)

(b)

Fig. 2. Measured DOP as a function of the area of detection. A_d ($= \pi d_2^2 / 4$) is the area of detection, where d_2 is the diameter of the second iris; A_s ($= \pi d_s^2 / 4$) is the average area of the coherence areas, where d_s is the average diameter of the coherence areas. (a) Measurements within a single coherence area, where $A_s = 171\,\text{mm}^2$. (b) Measurements over multiple coherence areas, where $A_s = 0.43\,\text{mm}^2$.

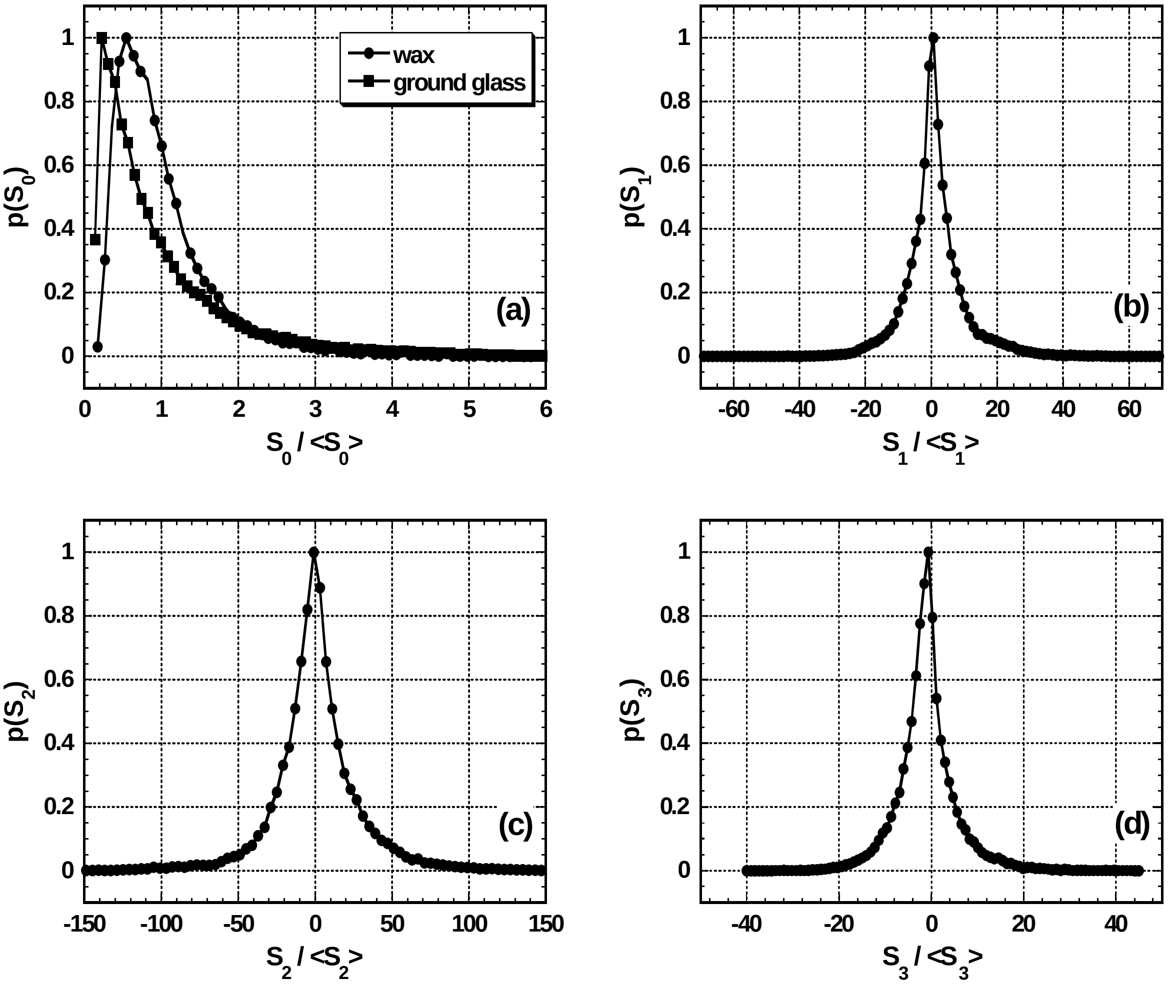

Fig. 3. Normalized probability density functions of Stokes parameters, which were measured in the speckle fields generated by the wax sample: (a) S_0, (b) S_1, (c) S_2, (d) S_3. The probability density function of the first Stokes parameter S_0 in the speckle field generated by the ground-glass sample is also given in (a) for comparison. $\langle S_0 \rangle$, $\langle S_1 \rangle$, $\langle S_2 \rangle$, and $\langle S_3 \rangle$ are the average values.

Figure 2(b) shows the DOP measured for multiple coherence areas. For both the ground-glass and the wax samples, the trends in Fig. 2(a) continued. It should be mentioned that the results in Figs. 2(a) and (b) were not joined together because the measurements were not made under the same conditions as a result of the replacement of the first iris.

From the Stokes vectors obtained with the ground-glass sample, it was found that the horizontally linear polarization state of the laser source was maintained in each measurement. In the measurements with the wax sample, a variation of the relative distribution of speckle intensity was observed with the CCD camera when the analyzer was rotated, indicating that the polarization states in the speckle field were non-uniformly distributed. Based on the effect of the scattering on light polarization, it is deduced that the multiple scattering events in the wax sample caused the distribution of polarization in the speckle field.

The probability density functions (PDFs) of Stokes parameters in the speckle field generated by the wax sample were investigated. Speckle patterns including multiple coherence areas were recorded with the CCD camera, which acted as a detector array. The Stokes parameters measured at each CCD pixel were taken for statistics. Figure 3 shows the probability density functions of the four Stokes parameters measured in the speckle field generated by the wax sample. The PDF of the first Stokes parameter, S_0, was similar to that obtained by Goodman[49] for the intensity of the sum of two speckle patterns, which was different from the negative exponential distribution of the fully-polarized speckle pattern. The other three PDF's were symmetrically distributed. For comparison, a PDF of the first Stokes parameter of a speckle pattern generated by the ground-glass sample is given in Fig. 3(a). It is seen that the distribution of this PDF is closer to the negative exponential distribution. Note that the DOPs corresponding to the two speckle fields in Fig. 3(a) are ~0.13 and ~0.99, respectively. The variation of the PDF with the DOP agrees with Goodman's theory.[49] According to Fercher *et al.*'s theory[50] in which the speckle field was described as a superposition of two fully developed uncorrelated linearly polarized speckle fields, the symmetrical distribution of the PDF of the second Stokes parameter indicates that the mean intensities of the two fields are the same.

Further, to well understand the phenomenon observed, I theoretically simulated the polarization states in speckle fields from a surface- and a volume-scattering medium, respectively. For the volume-scattering medium, both the polarization state and the phase of the transmitted optical field were assumed to be randomized by multiple scattering events. For the surface-scattering medium, only the phase of the transmitted optical field was assumed to be randomized as a result of the deformation of the phase front. In the simulation, the optical field at the first iris (D_1) was represented by a Jones vector:

$$\mathbf{E}(\xi,\eta)=\begin{bmatrix}E_x(\xi,\eta)\\E_y(\xi,\eta)\end{bmatrix}=\begin{bmatrix}E_{x_0}(\xi,\eta)e^{-j\phi_x(\xi,\eta)}\\E_{y_0}(\xi,\eta)e^{-j\phi_y(\xi,\eta)}\end{bmatrix}, \tag{6}$$

where $E_x(\xi,\eta)$ and $E_y(\xi,\eta)$ are two orthogonal components of the field, and (ξ, η) is the coordinate of a point in the plane where the first iris is located. A pupil function was applied to simulate the first iris, which gave the distribution of the optical field in the plane. For the surface-scattering medium, a horizontally linear polarization state with a constant E_{x_0} and a zero E_{y_0} was assumed, i.e.,

$$E(\xi,\eta)=\begin{bmatrix} E_{x_0}e^{-j\phi_x(\xi,\eta)} \\ 0 \end{bmatrix}, \tag{7}$$

and the phase $\phi_x(\xi,\eta)$ was assumed to be randomized. For the volume-scattering medium, assumptions were made: $\arctan(E_{y_0}(\xi,\eta)/E_{x_0}(\xi,\eta))$ was randomized between –π and π whereas the total optical intensity $(E_{x_0}{}^2(\xi,\eta)+E_{y_0}{}^2(\xi,\eta))$ remained constant, and the phases $\phi_x(\xi,\eta)$ and $\phi_y(\xi,\eta)$ were randomized as well. For both of the media, the phase was evenly randomized between –π and π. The two field components $E_x(\xi,\eta)$ and $E_y(\xi,\eta)$ were diffracted independently, which generated two independent speckle patterns in the far field. The diffraction processes were simulated by Fourier transforms:

$$E_x(x,y)=\mathrm{F}\{E_x(\xi,\eta)\}, \tag{8}$$

$$E_y(x,y)=\mathrm{F}\{E_y(\xi,\eta)\}, \tag{9}$$

where $E_x(x,y)$ and $E_y(x,y)$ are optical fields at the point (*x*, *y*) in the observation plane, and F{} denotes the Fourier transform. The final speckle pattern was generated by the summation of the two speckle patterns. The Stokes vectors of the speckle pattern were then calculated:

$$\begin{bmatrix} S_0 \\ S_1 \\ S_2 \\ S_3 \end{bmatrix}=\begin{bmatrix} E_x(x,y)E_x^*(x,y)+E_y(x,y)E_y^*(x,y) \\ E_x(x,y)E_x^*(x,y)-E_y(x,y)E_y^*(x,y) \\ E_x(x,y)E_y^*(x,y)+E_y(x,y)E_x^*(x,y) \\ j(E_x(x,y)E_y^*(x,y)-E_y(x,y)E_x^*(x,y)) \end{bmatrix}. \tag{10}$$

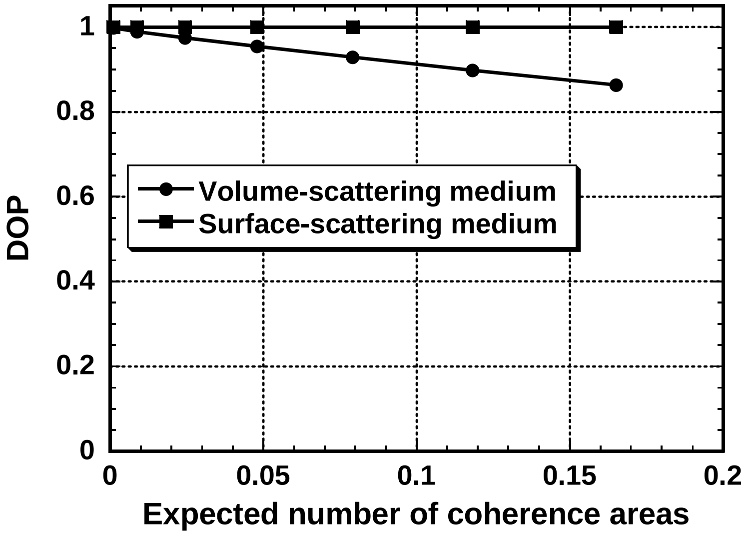

(a)

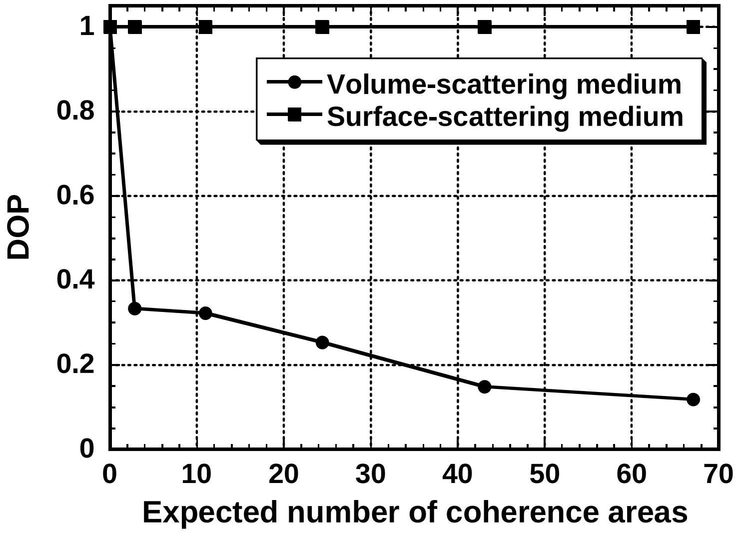

(b)

Fig. 4. Results of simulation, where the expected number of coherence areas is defined as the area of detection divided by the expected area of the coherence areas. (a) The variations of DOP within a single coherence area. (b) The variations of DOP over multiple coherence areas.

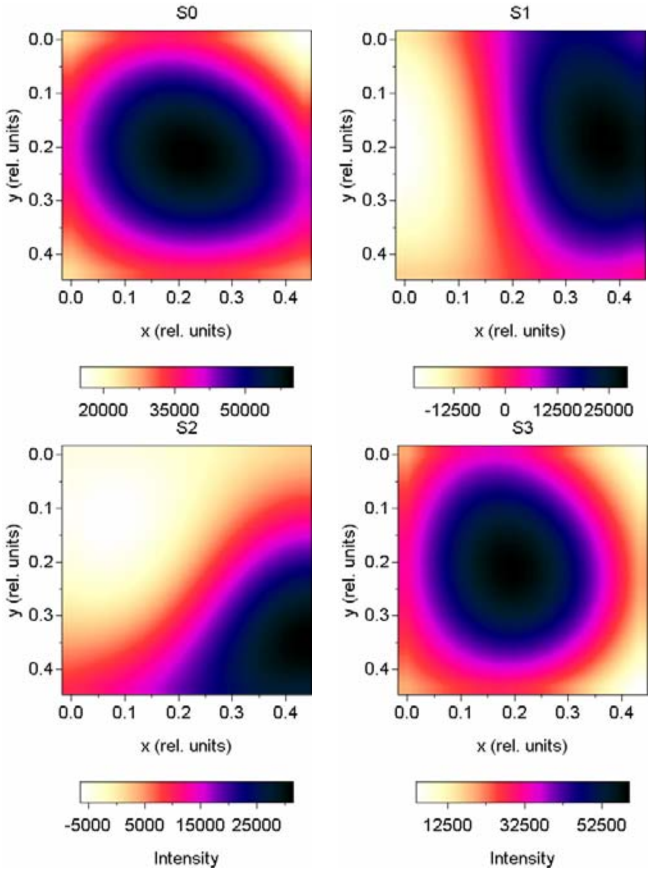

Fig. 5. The Stokes-vector components for a volume-scattering medium within a coherence area corresponding to the maximum in Fig. 4(a).

The results of simulation are shown in Fig. 4. Figure 4(a) shows the variations of the DOP with the size of detection area within a single coherence area. Figure 4(b) shows the results over multiple coherence areas. The simulation results agree with the experimental observation: a constant DOP of unity for the surface-scattering medium and a decreasing DOP for the volume-scattering medium as the area of detection increases. Because of the statistical nature of a speckle field, the experimental results and the simulation results can be compared only qualitatively. Figure 5 displays the four Stokes-vector components of a segment of the speckle field from the volume-scattering medium corresponding to the maximum area of detection in Fig. 4(a). It is clearly seen that the profiles are different among the four components. This agrees with the experimental observation from the wax sample and indicates that the Stokes vectors (polarization states) and the DOPs can vary from point to point in the speckle field, even within a single coherence area. This conclusion differs from the previous findings in speckle fields formed by light reflected from surface-scattering media.[56]

3. Discussion and summary

The results from the surface-scattering medium are obvious: because the speckle field is formed by the diffraction of an optical field with a single polarization state, the speckle field maintains the original polarization. For the volume-scattering medium, the independent diffraction processes of E_x and E_y create two orthogonal speckle fields polarized in the x and y directions, respectively. The vector sum of the two orthogonal speckle fields yields the total speckle field. Although the polarization states before diffraction are randomized, each point in the total speckle field has a DOP of unity because its resultant E_x and E_y components have a particular ratio of amplitude and a particular phase relation. Of course, the polarization states at different points in the total speckle field are statistically different from each other because both the ratio of amplitude and the phase between the two orthogonal speckle fields vary from point to point. The Stokes vector for an area including more than one such point is then determined by summing the Stokes vectors of all of the points in the area. As a result, the DOP of the area is less than unity and decreases statistically as the area is enlarged because more points are included in the enlarged area. It is worth noting that because of their statistical nature, polarization states and DOPs can be different even for detection areas of the same size.

It is concluded that the measured DOP in a speckle field that is generated by a volume-scattering medium depends on the size of the detection area: it decreases with an increasing area of detection, and only the DOP of an area much smaller than a coherence area is close to unity. This conclusion is important for the understanding of polarization phenomena in tissue optics, where polarized coherent light is applied and a speckle field is generated. When the DOP of a speckle field from a turbid medium such as biological tissue is measured, the above properties should be considered, especially if the measurement is made from a small area in the field. The fact that these parameters may vary statistically even for areas of the same size should be taken into account as well. Moreover, if a speckle field is observed in reflection mode from a piece of biological tissue, contributions from both the rough surface and the multiply scattering light should be considered.

It is useful to compare these conclusions with the DOP in a heterodyne detection scheme such as the one used in optical coherence tomography (OCT). It was found that the DOP in OCT maintains a value of unity as long as the scattering sample is stable during data acquisition regardless how many speckles are detected.[62] OCT is an amplitude-based detection system that uses an interference heterodyne. OCT detects the electric field of only the coherent part of the backscattered light. The electric field of the light from various locations on the detector surface is projected onto the analyzing polarization state and then added in amplitude. Equivalently, the electric field vectors of the light from the various locations of the detector are summed, and the vector sum is then projected onto the analyzing polarization state. As a result of this coherent-detection scheme in OCT, a DOP of unity is maintained despite scattering.

CHAPTER III

EXPERIMENTAL STUDY OF SIGNAL DETECTION SCHEMES FOR ULTRASOUND-MODULATED OPTICAL TOMOGRAPHY

1. Introduction

In ultrasound-modulated optical tomography, a laser beam is shone on a biological-tissue sample and an ultrasonic beam is focused into the tissue sample to modulate the transmitted light. Light passing through the ultrasonic beam will be modulated (also called as tagged, or encoded) by the ultrasound. Because the location of the ultrasonic beam is known, the origin of the tagged light can be obtained. By detecting the ultrasound-tagged light, the optical properties (absorption, scattering) in the ultrasonic column can be deduced. In the tomography, the imaging signal is the intensity of the modulated light. At a position of the ultrasound, a measurement is made to detect the signal. Scanning the ultrasound, position-dependent signal intensities are detected and an image is thus obtained. At the position of the object, the signal intensity drops because of the absorption or scattering of the object. The scattered light from the tissue forms speckles in the space. Each speckle spot is a coherence area. The bright spot or the dark spot contains modulated light and un-modulated light. The detection of the signal is therefore aimed to extract the modulated components from the un-modulated background. The modulated components have frequencies equal to the ultrasonic frequency or the harmonics.

In this chapter, three kinds of signal detection schemes were studied: optical-filtering based signal detection, parallel lock-in speckle detection and speckle contrast detection.

We call the latter two detections as multiple-detector detection, in which a CCD camera worked as multiple detectors.

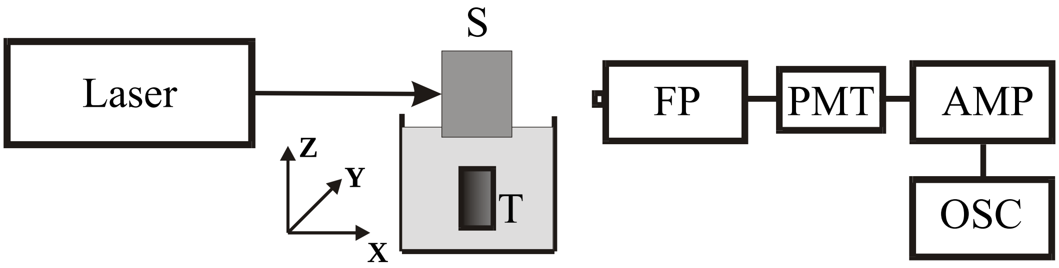

Fig. 6. Schematic of experimental setup for the optical-filtering based signal detection: S, sample; T, transducer; FP, Fabry-Perot interferometer; PMT, photomultiplier tube; AMP, pre-amplifier; and OSC, oscilloscope.

2. Optical-filtering based signal detection

In the detection, a Fabry-Perot interferometer was used as an optical filter and the intensity of ultrasound-modulated light was extracted through filtering out the background un-modulated light. Leutz *et al.*[19] had used a Fabry-Perot interferometer to measure the intensity spectra of ultrasound-modulated scattered light in their study of ultrasonic modulation mechanism. Here, the scheme was applied for imaging experiments.

2.1 Experimental setup

The experimental setup is shown in Fig. 6. Instruments included a 50-cm confocal Fabry-Perot interferometer (Burleigh 04054399) and a diode-pumped Nd:YAG laser (ADLAS, DPY325II, 532 nm). The Fabry-Perot interferometer provided a free spectral range (FSR) of 150 MHz. The laser source had a power of ~160 mW and a linewidth less than 7 MHz.

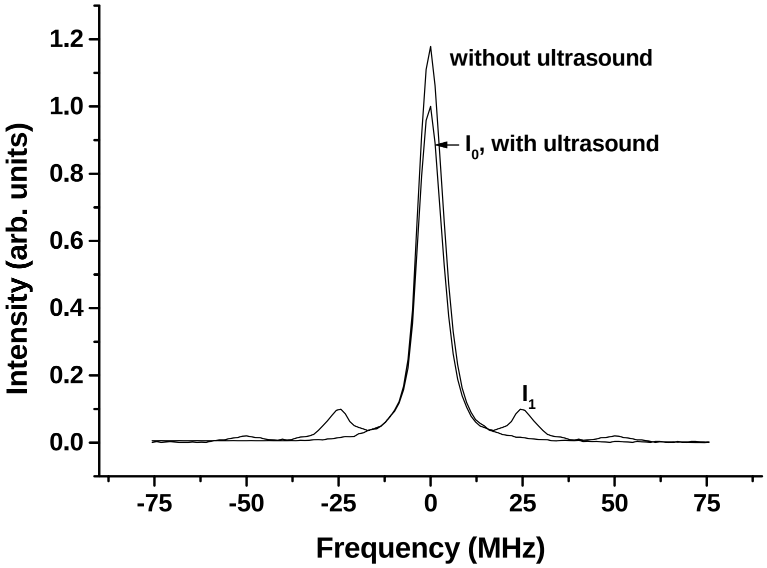

Fig. 7. Typical intensity spectra obtained with the Fabry-Perot interferometer in a highly concentrated gelatin phantom with a reduced scattering coefficient $\mu_s' = 15\,\mathrm{cm}^{-1}$. Two spectra obtained respectively with and without ultrasound (25 MHz) modulation are shown. I_1 and I_0 represent the intensities of the modulated component and the un-modulated component, respectively.

In the experiments, the laser beam was expanded to 30 mm in diameter to generate a power density of ~23 mW/cm^2 on a sample surface. A focused transducer was used for generating ultrasonic waves that were coupled into the sample through water. The ultrasonic waves were in burst mode and the peak pressures at the focal spot were in the range 10^5-10^6 Pa. Scattered light from the sample was collected with an optical fiber (not shown) into the Fabry-Perot interferometer, and at its exit, the light was detected with a photomultiplier (Hamamatsu R928). After being amplified by a low-noise preamplifier (Stanford Research Systems SR560), electrical signals were sent to a sampling oscilloscope (Tektronix TDS540B). The ultrasound-modulated signal, which carried the frequency of the ultrasound or its harmonics, was extracted.

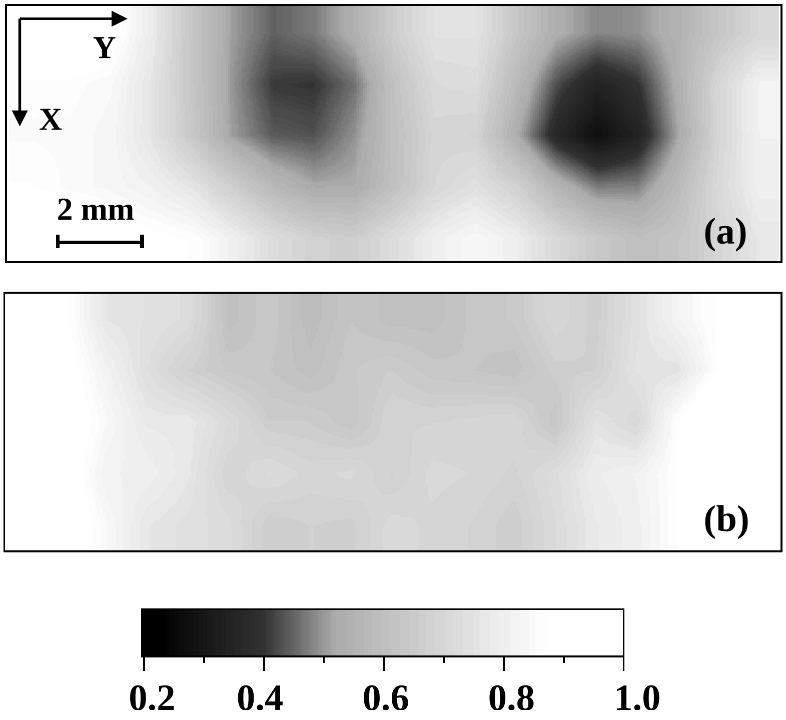

Fig. 8. 2D images of two ink-stained gelatin objects buried in a 30-mm-thick gelatin sample: (a) image obtained from the modulated signal; and (b) image obtained from the total light intensity. The reduced scattering coefficient of the tissue-simulating sample was 3 cm^{-1}.

2.2 Experimental results

Experiments based on the detection scheme were carried out with gelatin samples as turbid media. We prepared gelatin phantom by dissolving 10%-intralipid in 5% gelatin solutions. Typical intensity spectra are shown in Fig. 7, which were obtained with a 25-MHz transducer (Panametrics V324-SU, 19-mm focal length) in a 3-mm-thick concentrated sample with a reduced scattering coefficient $\mu_s' = 15\,\mathrm{cm}^{-1}$. When ultrasound is applied, intensity peaks corresponding to the modulated components appear in the spectrum, which are clearly separated from the main peak corresponding to the un-modulated background components. The ratio of the modulated component I_1 and the un-modulated component I_0, which represents the modulation depth, is high up to ~0.1. The intensities of the second harmonics of the ultrasound-modulated signals are also strong enough and are seen in the spectrum (at ± 50 MHz). The spectra in Fig. 7 were obtained after an average over twenty measurements, which show good SNRs in the experiment.

In imaging experiments, a 30-mm-thick gelatin sample was used, in which two cylindrical absorbent gelatin objects (3 mm in diameter and 11 mm in length) were buried. The host of the sample had the same reduced scattering coefficient as chicken breast tissues: $\mu_s' = 3\,\mathrm{cm}^{-1}$ at 532 nm. The absorbent objects were prepared by mixing India ink with a gelatin solution, which had an identical reduced scattering coefficient to the host. To obtain a 2D image, the sample was scanned along X and Y directions respectively. Figure 8(a) and (b) show 2D images obtained respectively with the modulation depth and the light intensity measured without ultrasound action. In the experiment, a 7.5-MHz transducer (Panametrics V321-SU, 19-mm focal length) was applied. The two objects are clearly discriminated in the image obtained with the ultrasonic modulation depth but they are not observable in the image obtained with the light intensity. The image contrast in Fig. 8(a) is high up to ~80%.

2.3 Discussion and conclusions

The preliminary experiments show that the optical-filtering based signal detection using a Fabry-Perot interferometer provides an efficient way of signal detection for ultrasound-modulated optical tomography. In conventional detections, scattered light is detected with a photo-electrical detector, e.g., photodiode or PMT, and the intensity of the ultrasound-modulated component is extracted from the electrical signals by use of signal processing. Because ultrasound-modulated components have random phases between different speckles, detecting multiple speckles with a single detector will result in a decrease of the measured modulation depth in conventional detections. As the dynamic range of a detection system is limited, the weak signal may not be detectable. So, single speckle detection usually is required in ultrasound-modulated optical tomography. On the other hand, the light intensity at detector surface usually is low in single speckle detection because the detector needs to be placed far away from the sample surface for detecting only one speckle. This usually leads to low signal-to-noise ratios in the detection. In comparison, in the optical-filtering based signal detection, the intensity of the ultrasound-modulated component is extracted directly in optical domain by the Fabry-Perot interferometer. The problem of the multiple speckle detection with a single detector is avoided, and the SNRs are high.

This detection scheme is more suitable for experiments using high frequency ultrasound. To be extracted efficiently from the un-modulated background, i.e., the main peak in the spectra, the ultrasound-modulated component should have frequency differences from the main peak as large as possible. This requires high frequency ultrasound to be applied. And, a laser source with a narrow linewidth, i.e., long coherence length, is desired. These in turn are the limitations for the efficacy of the detection scheme. As acoustic attenuation is increased with acoustic frequency, imaging with high-frequency ultrasound will be limited to shallow imaging. This detection scheme however is a promising signal-detection technique for ultrasound-modulated optical tomography, which is expected to play an important role in high resolution tomography that utilizes high frequency ultrasonic waves.

3. Parallel lock-in speckle detection[*]

The parallel lock-in speckle detection is, so far, the most efficient technique for ultrasound-modulated optical tomography. In this section, the detection scheme was studied. Four new methods were investigated for signal acquisition and analysis, in which laser speckle statistics was applied. The methods were compared with the previously used four-phase method in the imaging of all-biological-tissue samples. The four methods are: a three-phase method, two two-phase methods, and a cross-correlation method. The two-phase methods are similar to but different from Selb *et al.*'s approach.[63] Both Selb *et al.* and our group used two-acquisition detection schemes independently with different treatments. I proposed two methods for the two-acquisition detection. In the study, I compared the images with the commonly used four-phase method. The purpose of the study is, by a careful comparison of the methods, to find efficient ways for parallel speckle detection. In the experiments, two-dimensional images of all-biological-tissue samples in which the objects of interest were also biological tissues, were obtained. The

---

[*] Reprinted with permission from J. Li and L.-H. V. Wang, "Methods for parallel-detection-based ultrasound-modulated optical tomography," Appl. Opt. **41**, 2079-2084 (2002). Copyright 2002 Optical Society of America.

four methods had image quality comparable with the four-acquisition method but had advantages in shortening the acquisition time and improving the SNR.

3.1 Methods of signal acquisition and analysis

3.1.1 Four-phase method

In the parallel detection method, a source-synchronized lock-in technique is applied and a CCD camera is used as a detector array with each pixel acting as a single detector. The speckle size on the CCD surface is adjusted to match the pixel size. The signal in a single pixel can be expressed as

$$I = I_{dc} + I_{ac} \cos(\phi_s + \phi), \tag{11}$$

where I_{dc} is the background intensity; I_{ac} is the signal intensity related to the modulated ac signal; ϕ_s is the initial phase of the speckle; and ϕ is the phase delay of the signal applied to the ultrasonic transducer relative to the signal applied to the laser.

Traditionally in parallel detection, four acquisitions were made to recover the modulation signals, where the four sequential acquisitions have phase delays of 0°, 90°, 180°, and 270°, respectively. The signals from the four acquisitions are as follows:

$$I_1 = I_{dc} + I_{ac} \cos\phi_s, \tag{12}$$

$$I_2 = I_{dc} + I_{ac} \sin\phi_s, \tag{13}$$

$$I_3 = I_{dc} - I_{ac} \cos\phi_s, \tag{14}$$

$$I_4 = I_{dc} - I_{ac} \sin\phi_s. \tag{15}$$

From the above equations, one obtains

$$I_{dc} = (I_1 + I_2 + I_3 + I_4)/4, \tag{16}$$

$$I_{ac} = [(I_1 - I_3)^2 + (I_2 - I_4)^2]^{1/2}. \tag{17}$$

We define quantity $M = I_{ac} / I_{dc}$ as the modulation depth, which reflects the local optical and ultrasonic properties. After averaging the modulation depths obtained from all of the CCD pixels, the average <*M*> is taken as the imaging signal corresponding to the current location of the ultrasonic column. By comparing experimental data of $< I_{ac} / I_{dc} >$ and $< I_{ac} > / < I_{dc} >$, we found there was little difference, less than 0.1%, between the values. In practice, we take $< M > \approx < I_{ac} > / < I_{dc} >$.

3.1.2 Three-phase method

In this method, we simply reduce the number of acquisitions from four to three by making acquisitions at phase delays of 0^o, 90^o, 180^o or other combinations of three phases. From Eqs. 12–15, we get

$$I_{dc} = (I_1 + I_3)/2, \tag{18}$$

$$I_{ac} = [(I_1 - I_3)^2 + (2I_2 - I_1 - I_3)^2]^{1/2}, \tag{19}$$

for the combination of 0^o, 90^o, and 180^o, or,

$$I_{dc} = (I_2 + I_4)/2, \tag{20}$$

$$I_{ac} = [(I_2 - I_4)^2 + (2I_3 - I_2 - I_4)^2]^{1/2}, \tag{21}$$

for the combination of 90^o, 180^o, and 270^o.

In this case, the CCD images can be obtained as in the four-phase method. This method requires three acquisitions and consumes, therefore, three-fourths of the acquisition time required by the conventional four-phase method.

3.1.3 Two-phase method I

In this method, we further reduce the acquisitions from three to two, which can be done in either of two ways. In the first method, two acquisitions with a phase difference of 180^{o} are selected, e.g., 0^{o} and 180^{o}. From Eq. 12 and 14, one can obtain

$$I_{dc} = (I_1 + I_3)/2\,. \tag{22}$$

Subtracting Eq. 14 from Eq. 12 and squaring the result generates

$$4{I_{ac}}^2 \cos^2 \phi_s = (I_1 - I_3)^2\,. \tag{23}$$

Based on the speckle statistics that speckles have random phases, the average of $\cos 2\phi_s$ over the speckle field should be zero, and the average of $\cos^2 \phi_s$ over the speckle field should be 1/2:[49]

$$< \cos^2 \phi_s > = 1/2\,. \tag{24}$$

Averaging the variables in Eq. 23 for all CCD pixels and applying Eq. 24, we have

$$< {I_{ac}}^2 > = < (I_1 - I_3)^2 > /2\,. \tag{25}$$

In Selb *et al.*'s paper,[63] they extracted the item involving I_{ac} by subtracting two equations that were similar to Eq. 12 and Eq. 14, taking the absolute value of the difference, and using the relationship $<|\sin\phi_s|> = 2/\pi$. Our treatment is similar to but different from theirs.

To obtain the imaging signal $< M >$, approximation $< I_{ac} >^2 \approx < {I_{ac}}^2 >$ is applied, which is valid when variance ${\sigma_{I_{ac}}}^2$ (i.e., $< {I_{ac}}^2 > - < I_{ac} >^2$) is small compared with $< {I_{ac}}^2 >$ and $< I_{ac} >^2$.

$$< M > \approx < {I_{ac}}^2 >^{1/2} / < I_{dc} > = [< (I_1 - I_3)^2 > /2]^{1/2} / < (I_1 + I_3)/2 >\,. \tag{26}$$

Similarly, for the acquisitions with phase delays of 90° and 270°, the imaging signal is

$$< M > \approx < I_{ac}{}^{2} >^{1/2} / < I_{dc} > = [< (I_2 - I_4)^2 > /2]^{1/2} / < (I_2 + I_4)/2 > . \quad (27)$$

3.1.4 Two-phase method II

Alternatively, we can process the signals from the two-phase acquisitions by squaring Eq. 12 and averaging each variable over all the CCD pixels. Applying the statistical properties, i.e., Eq. 24, we obtain

$$< I_1{}^{2} > = < I_{dc}{}^{2} > + < I_{ac}{}^{2} > /2 , \quad (28)$$

and

$$< M > \approx (< I_{ac}{}^{2} > / < I_{dc}{}^{2} >)^{1/2} = [2(< I_1{}^{2} > / < I_{dc}{}^{2} > -1)]^{1/2} , \quad (29)$$

or

$$< M > \approx (< I_{ac}{}^{2} > / < I_{dc}{}^{2} >)^{1/2} = [2(< I_3{}^{2} > / < I_{dc}{}^{2} > -1)]^{1/2} , \quad (30)$$

where $I_{dc} = (I_1 + I_3)/2$ and approximation $< I_{ac} / I_{dc} > \approx (< I_{ac}{}^{2} > / < I_{dc}{}^{2} >)^{1/2}$ are applied. Modulation depth measured in a CCD pixel can be expressed as $I_{ac} / I_{dc} = < I_{ac} / I_{dc} > + \delta$, where δ (< 0, or, > 0) is the deviation of modulation depth I_{ac} / I_{dc} to the mean $< I_{ac} / I_{dc} >$. By squaring the equation, averaging over all CCD pixels, and ignoring the item involving $< \delta >$ and the item involving $< \delta^2 >$, we obtain the above approximation.

Similarly, for the combination of 90° and 270° phase delays, we have

$$< M > \approx (< I_{ac}{}^{2} > / < I_{dc}{}^{2} >)^{1/2} = [2(< I_2{}^{2} > / < I_{dc}{}^{2} > -1)]^{1/2} , \quad (31)$$

or

$$< M > \approx (< I_{ac}{}^{2} > / < I_{dc}{}^{2} >)^{1/2} = [2(< I_4{}^{2} > / < I_{dc}{}^{2} > -1)]^{1/2} , \quad (32)$$

where $I_{dc} = (I_2 + I_4)/2$. The two-phase methods would reduce by half the acquisition time compared to the four-phase method.

3.1.5 Cross-correlation method

In addition, we applied the correlation relationship for signal processing. Based on the above phase-delay parallel detection, we calculate the cross-correlation coefficients between the speckle patterns acquired with different phase delays. Because of the different phase delays, the speckle patterns will differ. The decorrelation of the speckle pattern between the two acquisitions reflects the effect of ultrasonic modulation if the decorrelation caused by Brownian motion is negligible within the acquisition time period. The cross-correlation coefficient between the *m*th and *n*th speckle patterns is calculated as

$$R_{m,n} = \sum_{i=1}^{N} (I_{m,i} - < I_m >)(I_{n,i} - < I_n >) / [\sum_{i=1}^{N} (I_{m,i} - < I_m >)^2 \sum_{i=1}^{N} (I_{n,i} - < I_n >)^2]^{1/2}, \quad (33)$$

where $m, n = 1, 2, 3, 4$; *N* is the number of pixels of the CCD camera; $I_{m,i}$ and $I_{n,i}$ are the signal intensity in the *i*th pixel in the *m*th and *n*th speckle patterns, respectively; and $<I_m>$ and $<I_n>$ are the average signal intensities of the *m*th and *n*th speckle patterns, respectively. The quantity $1 - R_{m,n}$ is taken as the imaging signal. Because only two acquisitions are required for correlation processing, the acquisition time is the same as in the two-phase method.

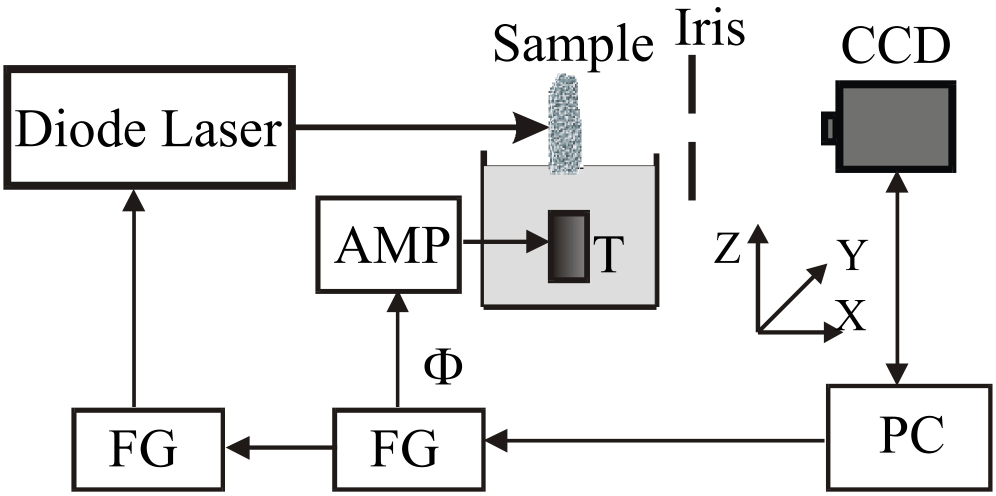

Fig. 9. Experimental setup: T, transducer; AMP, power amplifier; FG, function generator; PC, computer.

3.2 Experiments

3.2.1 Experimental setup

The experimental setup is shown in Fig. 9. A coordinate was given for reference. The optical axis was along the *X* axis, and the ultrasonic axis was along the *Z* axis. A diode laser of 690-nm in wavelength (Melles Griot, 56IMS667) was used as the light source. The coherence length of the laser was ~6 cm when it was modulated at 1 MHz. The laser beam incident upon the sample was ~8 mm in diameter and had a power of ~11 mW. Ultrasonic waves were generated by a focused ultrasonic transducer (UltranLab, VHP100-1-R38) with a 38-mm focal length in water and a 1-MHz central response frequency, and were coupled into the tissue sample through water in which the sample was partially immersed. The focal zone of the ultrasonic waves was ~2 mm in diameter and ~20 mm in length. The peak pressure at the focus was ~10^5 Pa, which is below the damage threshold for biological tissues. The light transmitted through the tissue generated speckle patterns, which were detected by a 12-bit digital CCD camera (Dalsa, CA-D1-0256T) with 256×256 pixels. The exposure time of the CCD camera was selected such that sufficient photons were collected. An iris was placed behind the sample to control the speckle size to approximately equal the CCD pixel size, which was about 16 μm. Two function generators (Stanford Research Systems, DS345) were used to drive the ultrasonic transducer and to modulate the diode laser, respectively. An RF amplifier (ENI, 325LA) was applied to amplify the signals driving the transducer. The two function generators shared the same time base for synchronization. The function generators and the CCD camera were controlled with a computer.

3.2.2 Experimental results and discussion

In the experiment, the source-synchronized lock-in technique was applied. The diode laser and the ultrasonic transducer were modulated at the same frequency of 1 MHz. The phase delay was set to a sequence of 0^o, 90^o, 180^o, and 270^o or one of 0^o, 180^o, 90^o, and 270^o. The different sequences did not show differences in the final results.

The host tissue samples were chicken-breast tissues and the buried objects were also chicken tissues—gizzards, which had a larger absorption coefficient and almost the same scattering coefficient as the chicken breast tissues. All of the methods described above were applied to imaging the samples. To obtain a two-dimensional image, we scanned the tissue sample along the X axis and Y axis.

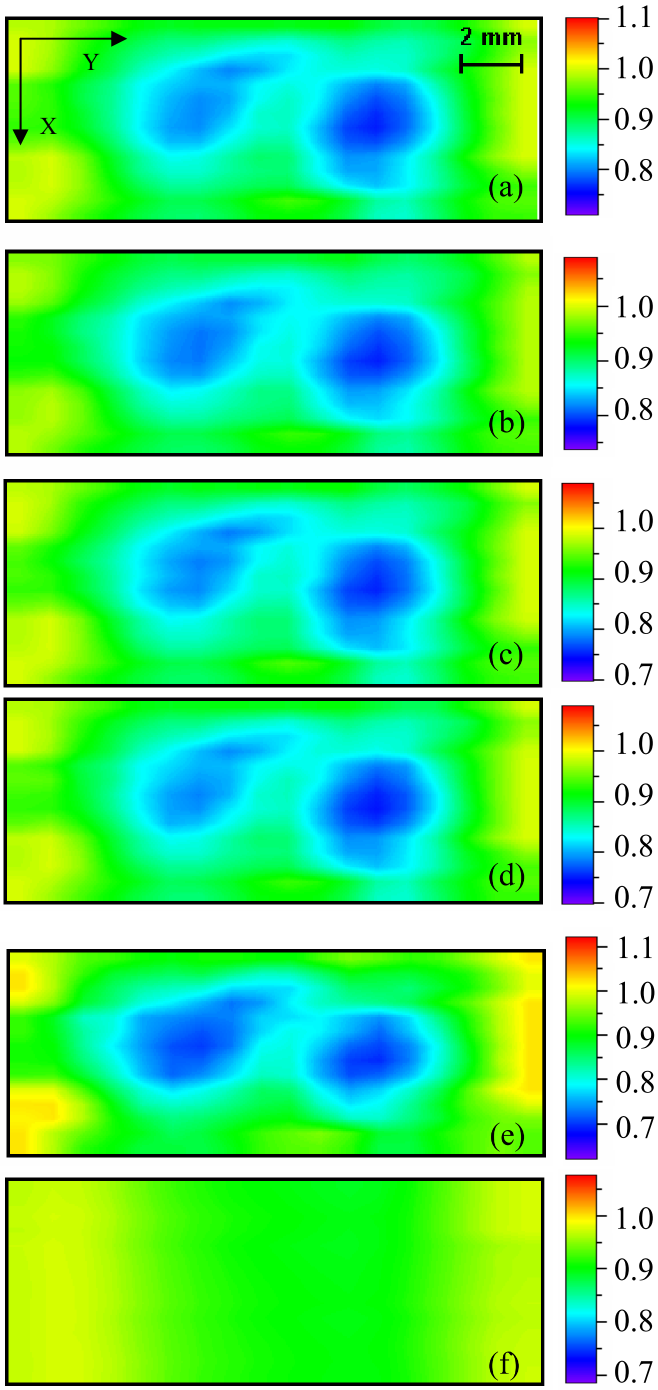

Fig. 10. Two-dimensional images of 15-mm-thick chicken-breast tissue in which two gizzard objects are buried. The images are obtained with: (a) four-phase method, (b) three-phase method, (c) two-phase method I, (d) two-phase method II, (e) cross-correlation method I, (f) dc signals.

Figure 10 shows a comparison of the 2D images obtained with the various methods. Figures 10(a) and 10(b) are images obtained with the four-phase method and the three-phase method, respectively. The combination of phase delays of 0^o, 90^o, 180^o was used in the three-phase method. Other combinations produced similar results. The sample was 15-mm thick in the X direction with two gizzard objects buried in the middle plane. The original sizes of the objects were approximately $1.5\,\text{mm} \times 2.5\,\text{mm} \times 7\,\text{mm}$ along the X, Y, and Z axes, respectively. The sizes changed after the sample was pressed with two parallel plates to maintain a uniform thickness in the X direction. In both images, the two objects are clearly seen, which indicates that the three-phase method—with less acquisition time—can generate an image with a quality close to that of the four-phase method.

Figures 10(c) and 10(d) show images obtained with two two-phase methods for the same sample. The images are from the acquisitions of the 0^o and 180^o phase delays: the images from the 90^o and 270^o phase delays are similar and are not shown. The images in Figs. 10(c) and 10(d) are almost the same and are similar to those from the four-phase method. The result justifies the approximations in Eqs. 26–27 and Eqs. 29–32, and shows that two-phase methods can be used as an alternative to the four-phase method to reduce acquisition time significantly.

Figure 10(e) is an image obtained with the cross-correlation method. The cross correlation of speckle patterns that were generated with 0^o and 90^o phase delays was studied. The image looks similar to those obtained with other methods.

Figure 10(f) gives an image using the average intensities of speckle patterns as the imaging signals, namely, an image from the dc signals ($< I > = < I_{dc} >$). The two objects are invisible in this image, while they are sharply visible in the images obtained with the modulated data—indicating the efficacy of spatial encoding using the focused ultrasonic beam.

To compare the image qualities in detail, 1D images corresponding to the scan line along the Y axis at the center of the sample are plotted. Figure 11(a) shows the 1D images obtained with the four-, three-, and two-phase methods, as well as one from the dc signals. It is apparent that the images obtained with the two-phase methods are almost the same as that obtained with the four-phase method. Detailed comparison shows that the contrast of images obtained with the three-phase method is lower than with the two- or four-phase methods. Figure 11(b) compares the 1D images obtained with the correlation coefficients calculated from the combinations of any two of the acquisitions of different phase delays. The images from different combinations are similar. Comparing Figs. 11(a) and 11(b) quantitatively, one can see that the contrasts of images obtained with the correlation method are slightly higher.

Since the images from the two-phase methods and the correlation method have qualities similar to those from the four-phase method, which has been employed in parallel detection, these methods are superior because they have the advantage of requiring half the acquisition time. It is recognized that speckle decorrelation due to the Brownian motion of scatterers needs to be avoided in parallel detection. A correlation time of 400 ms was measured in our experiments with 12-mm thick chicken tissues and the correlation time was found to decrease with the increase of tissue thickness. The data acquisition time must be shorter than the correlation time. However, sufficient exposure is needed in the case of low laser power or thick samples. Therefore, the reduction of acquisition time with the two-phase methods or the correlation method is significant.

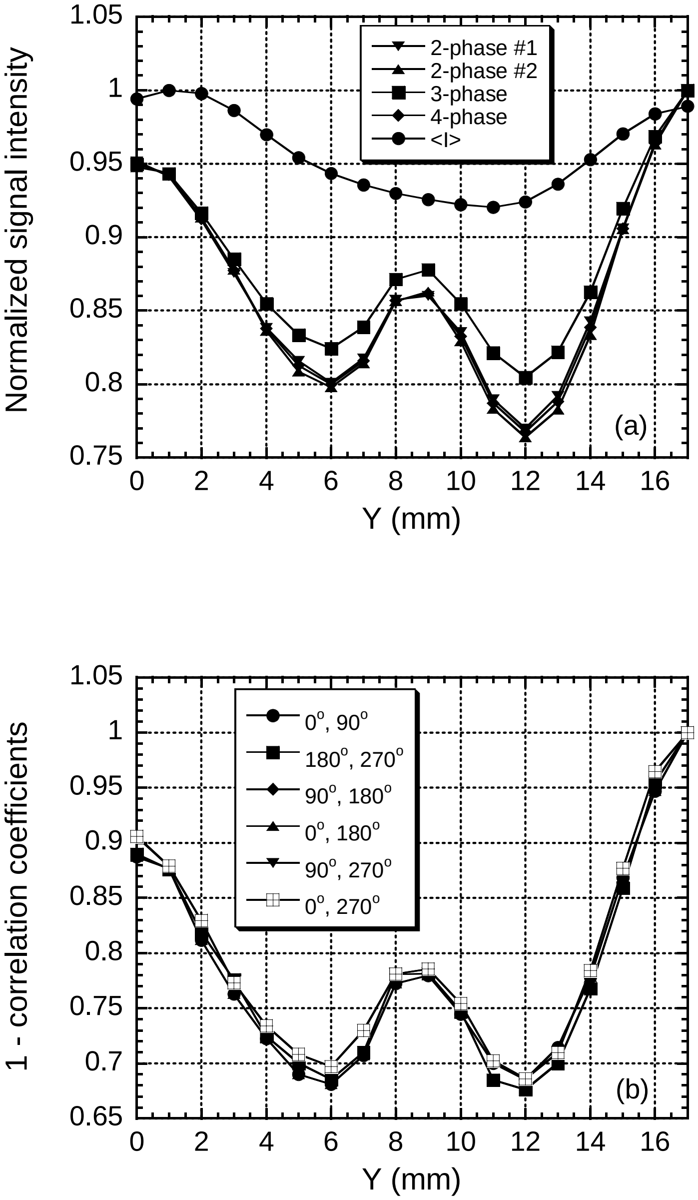

Fig. 11. Comparison of one-dimensional images. (a) Images obtained from four-phase, three-phase, and two-phase methods, as well as an image from the dc signals; (b) images from the cross-correlation coefficients, which were obtained from the various combinations of two different phase-delay acquisitions.

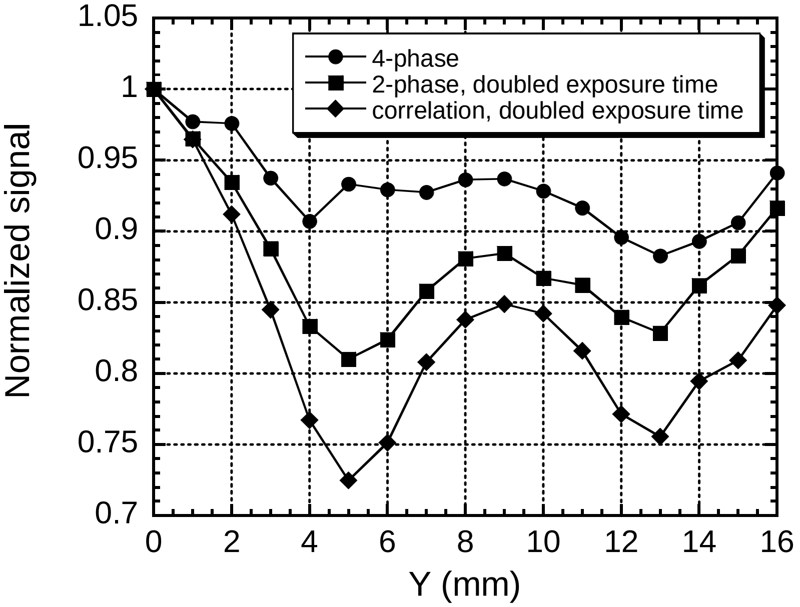

Fig. 12. Comparison of images obtained with the four-phase method, two-phase method, and cross-correlation method, respectively. The exposure time in the two-phase method and cross-correlation method was doubled.

In terms of the SNR, the two-phase methods and the correlation method yield higher SNR than the four-phase method. With the same acquisition time, the exposure time of each acquisition in the two-phase methods or the correlation method can be two times as long as that in the four-phase method. The increase of exposure time will increase the SNR. Figure 12 shows a comparison of the 1D images obtained with the four-phase method, two-phase method and cross-correlation method, respectively, where the last two methods had a doubled exposure time. The measurements were made with another chicken-tissue sample which was ~16 mm thick. It is shown that the SNR improvement with the two-phase method or with the cross-correlation method also enhanced the image contrast. The figure shows that the image contrast obtained with the cross-correlation method was higher than that obtained with the two-phase method, which agrees with the result shown in Figure 11. This implies that the correlation method has higher sensitivity in detecting the ultrasonic modulation.

Moreover, we compared images obtained with our two two-phase methods and with Selb *et al.*'s method.[63] The comparison shows that the three different two-phase methods produce images with similar qualities.

3.3 Conclusions

This research extends the study of ultrasound-modulated optical tomography based on parallel speckle detection. In an effort to improve upon the conventional four-phase method, four methods of signal acquisition and analysis were studied. The imaging experiments utilized all-biological-tissue samples: chicken-breast tissues in which two objects of chicken gizzard were buried.

Comparison of the resulting images shows that, with the same exposure time for each acquisition, these methods produce images with a comparable quality to those produced by the four-phase method, but with a reduced total acquisition time. Likewise, the exposure time in the two-phase methods or the correlation method can be two times as long as that in the four-phase method. Significant improvements of the SNR, i.e., image quality, through the use of the two-phase method and the cross-correlation method were observed. It is concluded that these methods are superior to the four-phase method and should be applied to ultrasound-modulated optical tomography.

4. Speckle contrast detection*

All of the imaging techniques applied in ultrasound-modulated optical tomography are based on the detection of ultrasound-tagged light. Among these techniques, the parallel detection is the most efficient technique. However, in the parallel detection, because four or two acquisitions are needed to obtain imaging information of a location at the ultrasonic column and each acquisition has to collect sufficient photons to maintain enough SNR, the long acquisition time involved may lead to speckle decorrelation.

In this section, an imaging method based on the detection of laser-speckle contrast was investigated. In purely optical imaging, Thompson *et al.*,[64] McKinney *et al.*[65] and Naulleau *et al.*[66] have applied speckle contrast in the imaging of scattering media in transmission geometries. And in the biomedical field, speckle contrast has been used in the optical characterization of surface roughness[67] and in the detection of skin disease in lightly scattering thin samples.[68] Jacques *et al.*[69] used speckle contrast in the acoustically modulated speckle imaging of biological tissue surfaces. Their experiment was somewhat similar to our experiments in that acoustic waves were applied and speckle contrast was measured. But Jacques *et al.* did the experiment using reflection geometry, at lower acoustic frequencies (0–30 Hz), and, most differently, the acoustic modulation was not used for improving spatial resolution. The purpose of their experiment was to discriminate superficial tissue layers, which had different mechanical properties and thus had different laser speckle patterns in response to mechanical driving forces from the acoustic waves. The technique proposed here is intended to image objects buried deeply

---

[*] Reprinted with permission from J. Li, G. Ku, and L.-H. V. Wang, "Ultrasound-modulated optical tomography of biological tissue using contrast of laser speckles," Appl. Opt. **41**, 6030-6035 (2002). Copyright 2002 Optical Society of America.

in biological tissues by taking advantage of ultrasonic resolution. It is a case of transmission geometry, and the image contrast is based on the optical properties of the tissues.

In the study, experiments showed that when ultrasound acted on the tissues, the contrast of the speckle pattern formed by the transmitted light decreased. The ultrasound-dependent speckle contrast could be used for tissue imaging. By measuring the variation of the speckle contrast with the location of ultrasonic column, one could detect optical inhomogeneities inside the tissue even if the tissue is acoustically homogeneous. Using this technique, 2D images of biological tissue samples with thicknesses of up to 25 mm were obtained. It was demonstrated that the technique was not significantly influenced by speckle decorrelation, that it could be easily implemented, and that it produced better image contrast than the parallel detection technique.

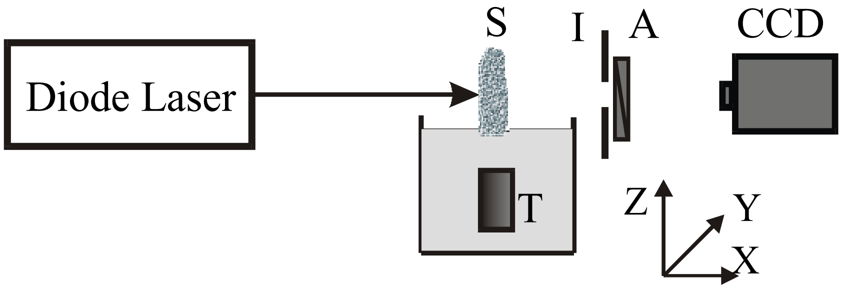

Fig. 13. Experimental setup: S, sample; I, iris; A, analyzer; and T, transducer.

4.1 Experiment

The experimental setup is shown in Fig. 13, in which a coordinate system is given for reference. The optical axis was along the *X* axis and the ultrasonic axis was along the *Z* axis. A diode laser (Melles Griot 56IMS667, 690-nm wavelength) was used as the light source. The coherence length of the laser without modulation was more than 1 m. The laser beam incident upon the sample was ~8 mm in diameter and had a power of ~24 mW. Ultrasonic waves were generated by a focused ultrasonic transducer (Ultran VHP100-1-R38) with a 38-mm focal length in water and a 1-MHz central response frequency. They were coupled with the tissue sample through water in which the sample was partially immersed. The focal zone of the ultrasonic waves was ~2 mm in diameter and ~20 mm in length. The light transmitted through the tissue generated a speckle pattern, which was detected by a 12-bit digital CCD camera of 256×256 pixels (Dalsa CA-D1-0256T). The exposure time of the CCD camera was set to ensure that sufficient photons were collected. An iris was placed behind the sample to control the average speckle size D_s on the CCD surface, with the relationship $D_s \propto \lambda L / D_i$, where λ was the light wavelength; L was the distance between the iris and the CCD surface; and D_i was the iris aperture. An analyzer was applied to enhance the speckle contrast.

The speckle contrast of a speckle pattern is defined as the ratio $\sigma_I / <I>$, where σ_I is the standard deviation of intensity in the pattern and $<I>$ is the mean of the intensity. In the experiments, fifty measurements were averaged to improve the SNR. To obtain 2D images, the sample was mechanically scanned with a translation stage along the X and Y directions.

4.2 Results and Discussion

To obtain high speckle contrasts, the iris aperture was adjusted to match the speckle size to the CCD pixel size, which was 16 μm. It was found that there was a tradeoff between the speckle contrast and the light intensity detected by the CCD camera. Figure 14 shows the variations in the speckle contrast and the light intensity with the size of the iris aperture. Results obtained with and without a polarizer are both shown in the figure. It can be seen that with a decrease in the aperture (namely, with an increase of the speckle size), the speckle contrast increased, whereas the light intensity decreased. With a polarizer, a higher speckle contrast could be achieved but the light intensity was much lower. Taking into account the fact that at low intensities the SNR in the detection was low because of the influences of the shot noise and the dark-current noise, most measurements were conducted without a polarizer and with larger iris apertures to keep sufficient SNRs. The speckle contrasts measured in the experiments therefore were relatively low, ~0.14.

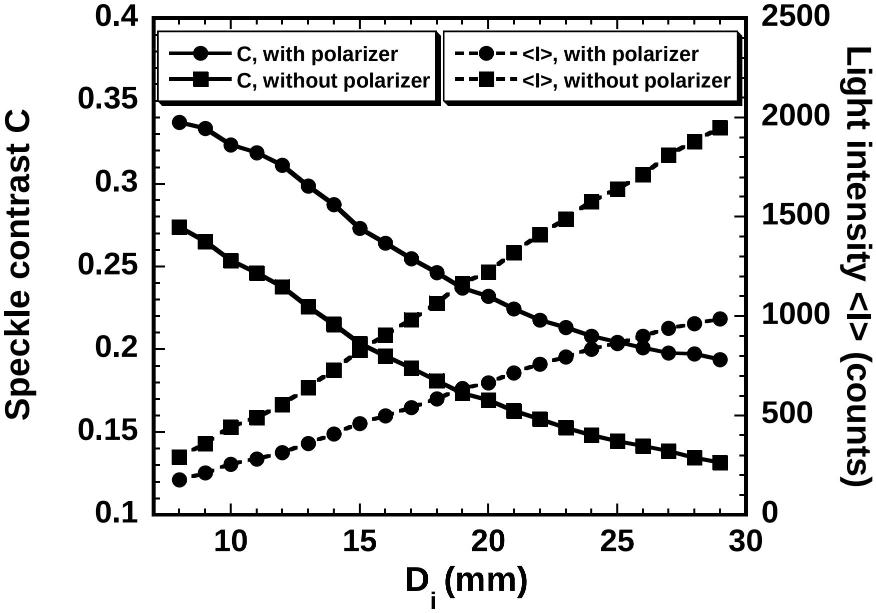

Fig. 14. Variations of measured speckle contrasts and light intensities <*I*> with the iris aperture D_i. The results obtained with and without a polarizer are compared.

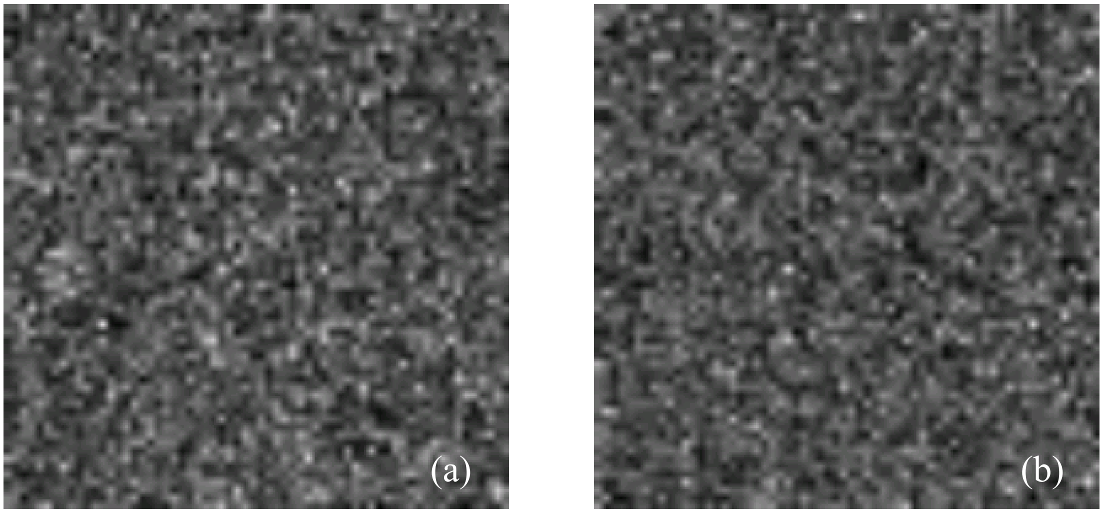

Fig. 15. Speckle patterns measured with the CCD camera. (a) Without ultrasonic modulation, speckle contrast is 0.146; (b) With ultrasonic modulation, speckle contrast is 0.138.

Figure 15 shows two speckle patterns measured when the ultrasound respectively was and was not applied to a chicken tissue sample. Although the change was not visually distinct in Fig. 15(b), the calculation of the speckle contrast showed that the speckle contrast was lower when the ultrasound was applied. The variation of speckle contrast with ultrasound intensity was studied. The result is shown in Fig. 16. With increasing the input power of the transducer, the speckle contrast decreased rapidly, showing a nearly linear dependence on the input power. The stability of speckle contrast was checked, which was over 99% within 20 minutes under a stable condition. So, speckle contrast, which is subject to ultrasound influence, can be used to reflect the ultrasonic modulation of scattered light. That is, it can be used for ultrasound-modulated optical tomography. In the experiments in order to generate efficient ultrasonic modulation with ultrasound pressures within the safety limit for biological tissues, an input power of ~280 mW was applied, which generated ultrasonic pressures of ~10^5 Pa at the focal spot.

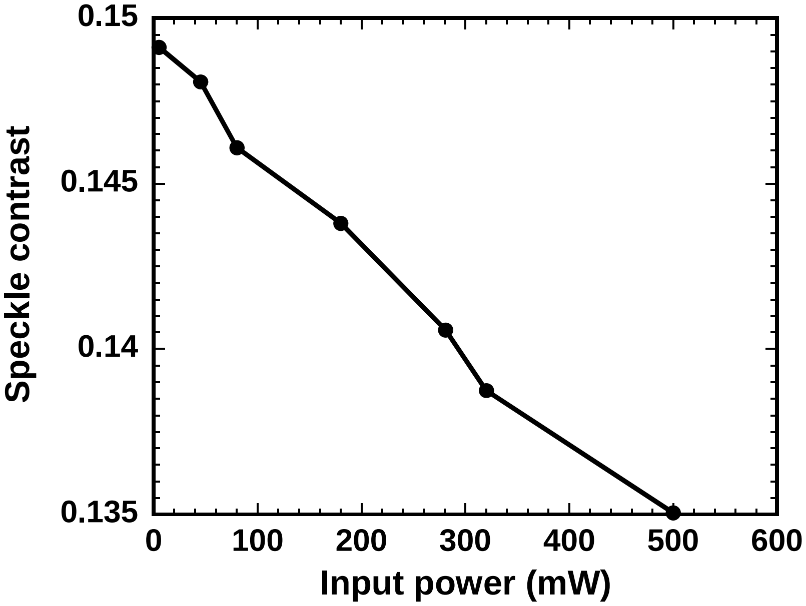

Fig. 16. Variation of speckle contrasts with the input power of the transducer.

The tissue samples used in the experiments were skinless chicken breast (muscle) tissues, with thicknesses ranging from 15 to 25 mm. Two kinds of optically absorbent objects were used respectively: soft rubber and chicken gizzards. The soft rubber has good acoustic coupling with tissue and has little acoustic absorption. The samples with gizzard-objects were all-biological-tissue samples. An ultrasound exam of such a sample with a clinical ultrasonic imager showed that gizzard had almost the same acoustic impedance as chicken breast tissue. The optical coefficients of chicken breast tissue and the gizzard objects were measured with our oblique-incidence reflectometry.[70] The gizzard showed nearly two times as much absorption but almost identical scattering as the chicken breast tissue.

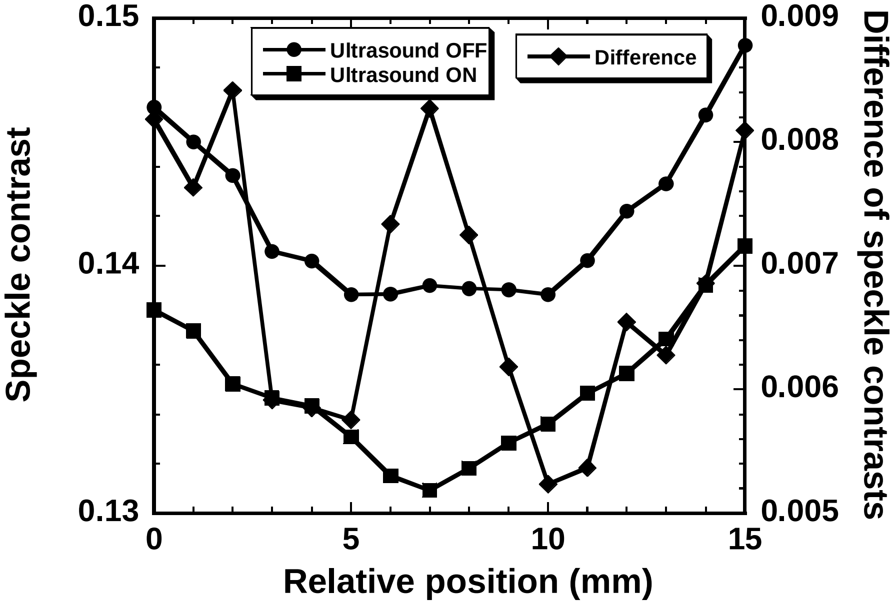

Fig. 17. Comparison of 1D images of two rubber objects, which were obtained respectively from speckle contrasts measured with and without ultrasonic modulation and from the difference of the speckle contrasts.

In the experiments, the speckle contrasts under two conditions: with and without ultrasonic modulation were measured. Figure 17 shows a comparison of three 1D images. In two of them, speckle contrasts were taken as imaging signals, which were measured respectively with and without ultrasonic modulation. In the third one, differences of the speckle contrasts were taken as imaging signals. The sample was a 15-mm-thick chicken breast tissue, in which two rubber objects were buried. The objects are not seen in the two images obtained directly from the speckle contrasts but they are clearly seen in the image produced by the difference between the two. Subtraction between the speckle contrasts eliminated background contributions and thus provided good imaging signals.

Figure 18(a) shows a sketch of a 25-mm-thick chicken breast tissue sample containing two rubber objects, which were buried in the middle plane along the *X* axis and separated away along the *Y* axis by about 6 mm. The sizes of the two objects were about $1.9\times3.1\times10$ mm^3 and $2.1\times3.1\times10$ mm^3, along the *X*, *Y* and *Z* axes, respectively. Figure 18(b) shows an image obtained with the speckle contrast detection. The objects are clearly seen in the image. For comparison, the mean intensity $< I >$ of the speckle pattern as well as the speckle contrast obtained without ultrasonic modulation was also used as imaging signals, and the images are shown in Figs. 18(c) and (d), respectively. The objects are not visible in these two cases. Figure 18(c) shows that the detected light intensity could not directly generate an image of the buried objects. Figure 18(d) shows a result similar to that in Fig. 17, indicating that the speckle contrasts obtained without ultrasonic modulation could not generate images of buried objects. In this case, the imaging in fact was purely optical imaging, just like that taken by Thompson *et al.*,[64] whereas the objects used here were absorbent media instead of scattering media. Figure 18 shows that ultrasonic modulation in speckle-contrast imaging acts similarly to the way it acts in other modalities of ultrasound-modulated optical tomography—it provides spatial resolution.

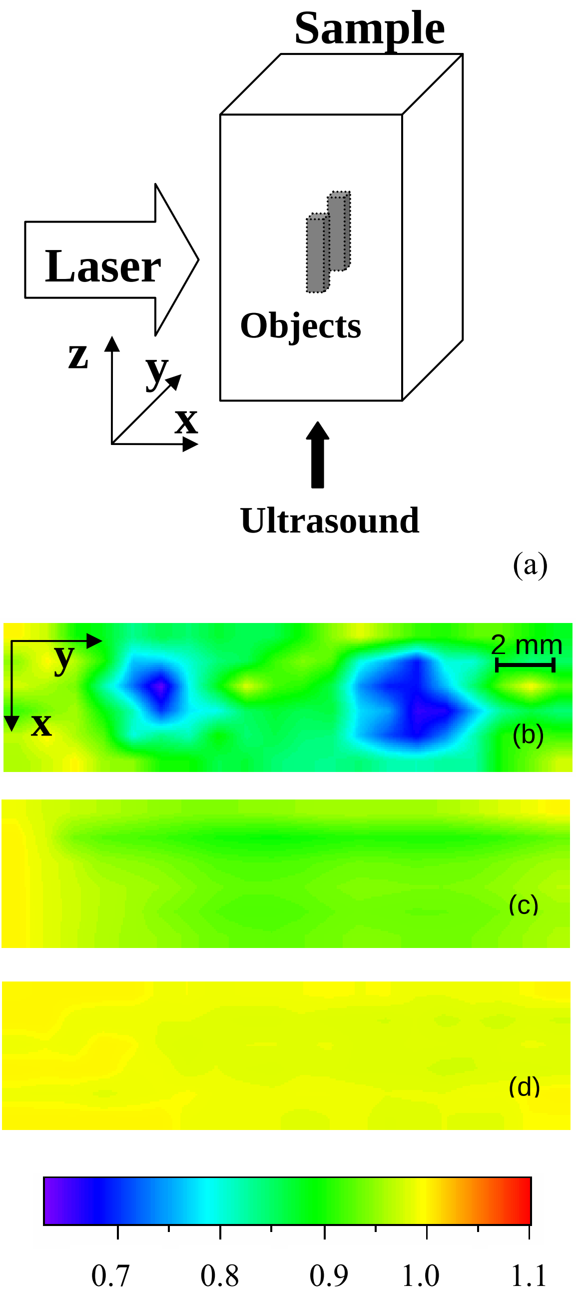

Fig. 18. (a) Sketch of a 25-mm-thick chicken breast tissue sample containing two rubber objects; (b) Image obtained from the difference of speckle contrasts measured with and without ultrasonic modulation; (c) Image obtained from the mean intensity of speckle pattern; (d) Image obtained from the speckle contrast measured without ultrasonic modulation.

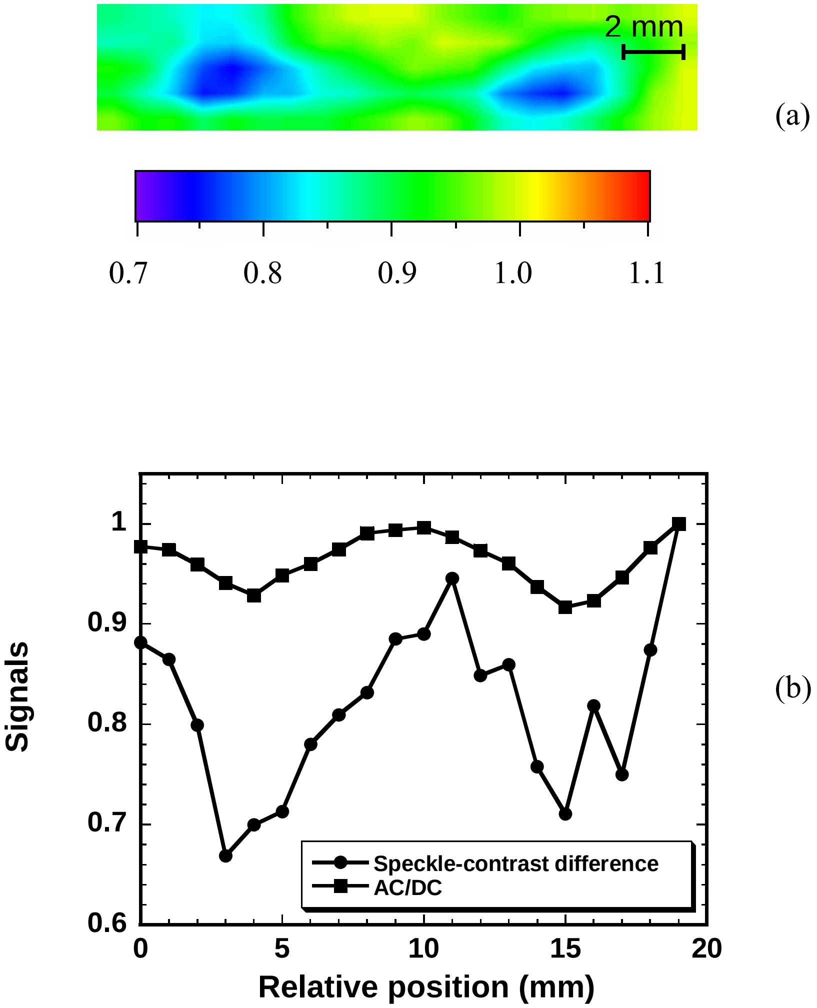

Fig. 19. (a) 2D images of two gizzard objects buried in a 17-mm-thick chicken breast tissue sample. (b) Comparison of 1D images obtained respectively with speckle-contrast detection and parallel detection. AC/DC is the signal obtained in the parallel detection.

Figure 19(a) shows a 2D image of a 17-mm thick sample with two buried gizzard objects. The original sizes of the two objects were about 2×3×8 mm^3 and 2×3×10 mm^3, respectively. The sizes were changed after the sample was pressed with two parallel planes to maintain a uniform thickness in the *X* direction. The objects are sharply visible in the image. With the same sample, we did imaging using parallel detection and compared the results. Figure 19(b) presents the 1D images obtained by use of parallel detection and speckle contrast detection, respectively. The two experiments were conducted with the same laser intensity and ultrasound intensity. In the figure, AC/DC represents the imaging signal in parallel detection. Both the AC/DC and the speckle-contrast difference are normalized. It can be seen that the image contrast obtained with the present technique is much higher; in fact, it is about three times as high as that obtained with parallel detection. It is also shown that the signal fluctuation was more significant in the speckle-contrast detection. One possible reason for the observed fluctuation is that the number of measurements was not sufficient. In the experiments, we obtained one contrast value from each measurement. The average over 50 measurements might not have been sufficient to reduce the fluctuation.

The proposed detection technique utilizes the influence of ultrasonic modulation on speckle-intensity contrasts. When ultrasound interacts with laser light passing through tissues, it modulates the light through the modulation of displacements of scatterers and the index of refraction. The modulation causes the speckle intensity detected by a certain pixel of the CCD camera to fluctuate at the ultrasound frequency as well as its harmonics. We derived the relationship between the speckle contrast and the ultrasonic modulation depth. The light intensity on a pixel of the CCD camera can be expressed as:

$$I = I_b + I_m + 2\sqrt{I_b I_m}\cos(\omega_a t + \Delta\varphi)\,, \tag{34}$$

where I_b, I_m are the intensities of un-modulated light and modulated light, respectively, ω_a is the ultrasonic frequency, and $\Delta\varphi$ is the phase difference between the un-modulated light and the modulated light. Because the CCD camera runs at low frequencies, the intensity recorded by the camera is time-averaged, which is given by

$$\bar{I} = I_b + I_m + \frac{1}{T}\int_0^T 2\sqrt{I_b I_m}\cos(\omega_a t + \Delta\varphi)dt\,, \tag{35}$$

where T is the CCD exposure time. Averaging Eq. (35) over the speckle field, with the statistical property of the speckle pattern,[49] i.e., $\langle \sin(\Delta\varphi)\rangle = 0$, we obtain a spatially-averaged intensity:

$$\langle \bar{I} \rangle = \langle I_b \rangle + \langle I_m \rangle\,, \tag{36}$$

and

$$\langle \bar{I}^2 \rangle = \langle I_b{}^2 \rangle + \langle I_m{}^2 \rangle + 2\langle I_b I_m \rangle + 2\sin^2(\frac{\omega_a T}{2})\left(\frac{2}{T\omega_a}\right)^2 \langle I_b I_m \rangle\,, \tag{37}$$

where $\langle\ \rangle$ represents the spatial-average operation. The variance of the intensity σ^2 and the speckle contrast C are thus obtained:

$$\sigma^2 = \langle \bar{I}^2 \rangle - \langle \bar{I} \rangle^2 = \langle I_b{}^2 \rangle - \langle I_b \rangle^2 + \langle I_m{}^2 \rangle - \langle I_m \rangle^2 + 2\sin^2(\frac{\omega_a T}{2})\left(\frac{2}{T\omega_a}\right)^2 \langle I_b I_m \rangle \tag{38}$$

$$C = \frac{\sigma}{\langle \bar{I} \rangle} = \frac{\sqrt{C_b{}^2 + C_m{}^2 M^2 + 2\sin^2(\omega_a T/2)(2/T\omega_a)^2 M}}{1+M}\,, \tag{39}$$

where,

$$C_b = \frac{\sqrt{\langle I_b{}^2 \rangle - \langle I_b \rangle^2}}{\langle I_b \rangle}\,, \tag{40}$$

$$C_m = \frac{\sqrt{\langle I_m{}^2 \rangle - \langle I_m \rangle^2}}{\langle I_m \rangle}\,, \tag{41}$$

and

$$M = \frac{\langle I_m \rangle}{\langle I_b \rangle}. \tag{42}$$

M is the ultrasonic modulation depth. C_b and C_m can be considered as contrasts of two speckle fields with mean intensities of $\langle I_b \rangle$ and $\langle I_m \rangle$, respectively. Because we used 1-MHz ultrasound and ~20 ms CCD exposure time in the experiments, i.e., $1/T\omega_a << 1$, and the modulation depth was much less than unity, the 2nd and 3rd terms in the numerator in Eq. (39) are small and thus can be ignored. The speckle contrast can be expressed as

$$C \approx \frac{C_b}{1+M}, \tag{43}$$

which shows that the speckle contrast decreases approximately linearly with the increase of the ultrasonic modulation depth.

According to the analysis of ultrasonic modulation, it can be determined that the modulation depth is proportional to the square of the ultrasonic amplitude; namely, the modulation depth is proportional to the ultrasonic power or electric power input to the transducer. By combining this relationship and Eq. (43), the approximately linear decrease in the speckle contrast with the power input in Fig. 16 can be explained.

If a portion of the incident light is absorbed by objects located inside the ultrasonic column, the influences of ultrasound on the light and, as a consequence, on the speckle contrast are weakened. That is, the speckle contrast decreases less. Therefore the variation in speckle contrast can provide information for imaging. Further, the differences in those speckle contrasts that are obtained with and without ultrasonic modulation provide image signals directly. By scanning the sample, one can obtain images having spatial resolution determined by the focal spot of the ultrasound. Purely optical imaging based on speckle contrasts was successfully demonstrated in Thompson *et al*'s experiments on imaging a scattering object.[64] In our experiments, however, it was found that purely optical imaging was not efficient for detecting absorbent objects. The results show that with ultrasonic modulation, the speckle contrast can be used for imaging absorbent objects. In the experiments, objects with strong optical absorption properties were used, which gave satisfactory image contrasts. If the objects had been less absorbent, the image contrast would have been lower. Since the measured signal, i.e., the speckle-contrast difference, is small, imaging less-absorbent objects will be more challenging. In future studies, an objective will be to improve the detection method in order to more efficiently image low contrast objects.

When using parallel detection, one should be careful with the speckle decorrelation caused by the Brownian motion of scatterers, which may occur during the four- or two-acquisition measurement period. It has been mentioned that the correlation time was found to decrease with the increase of tissue thickness. In the parallel detection, the total data-acquisition time must be shorter than the correlation time. However, sufficient exposure is needed in the case of low laser power or thick samples. With the present technique, acquisitions with and without ultrasonic modulation at a location can be nearly independent and the speckle decorrelation can be avoided if each acquisition time is short enough. Compared with parallel detection, the present technique requires fewer components and is easy to conduct.

4.3 Conclusions

Using the speckle-contrast mechanism in ultrasound-modulated tomography, 2D images of biological-tissue samples up to 25 mm thick were obtained. The technique is superior to speckle-contrast-based purely optical imaging because it can discriminate absorbent objects by taking advantage of ultrasonic resolution. Comparison showed that images obtained with this technique had better contrast than those obtained with parallel detection and that speckle decorrelation was less significant in the detection. In addition, the present technique was simple to setup. This technique, combining speckle contrast detection with ultrasonic modulation, provides an efficient method for ultrasound-modulated tomography of biological tissues.

CHAPTER IV

TOMOGRAPHY OF THICK BIOLOGICAL TISSUES WITH TRANSMISSION- AND SIDE-DETECTION CONFIGURATIONS[*]

1. Introduction

To meet the requirements of practical applications, it is required to improve imaging depth in ultrasound-modulated optical tomography. In this chapter, experimental study was made on thick-biological-tissue tomography. Speckle decorrelation was studied, and time-dependent correlation coefficients of speckle patterns were measured at various sample thicknesses. The corresponding speckle contrasts of the speckle patterns were checked. Through the use of speckle-contrast detection that has been described in the previous chapter, to which some improvements were added, imaging experiments with tissue samples of thicknesses ranging from 40 to 50 mm in a transmission-detection configuration were implemented. In addition, side-detection configurations were proposed. Images obtained with side-detection configurations were compared with those obtained with transmission-detection configuration as well as with those obtained with reflection-detection configuration (reported by other researchers). For the side-detection configuration technique, initial experiments were carried out to check the sensitivity of ultrasound-modulated optical tomography for discriminating objects of different optical absorption properties and for measuring distributions of the ultrasound-modulated signal inside a tissue sample to characterize the tissue's optical properties.

---

[*] Reprinted with permission from J. Li, S. Sakadžić, G. Ku, and L.-H. V. Wang, "Transmission- and side-detection configurations in ultrasound-modulated optical tomography of thick biological tissues," Appl. Opt. **42**, 4088-4094 (2003). Copyright 2003 Optical Society of America.

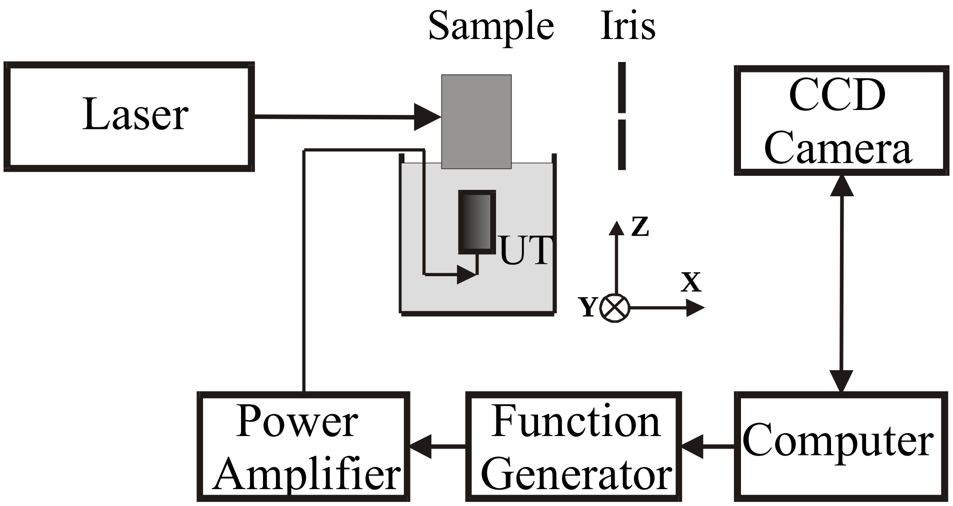

Fig. 20. Schematic of experimental setup: UT, ultrasonic transducer.

2. Experimental setup

The setup, which is similar to that described in the previous chapter, is shown in Fig. 20. In the present experiments, a tunable Ti:Sapphire laser (Coherent Inc. 890) operating at 786 nm was applied; we took advantage of its power (~140 mW) and its coherence length (over 30 m). The laser beam was expanded to ~14 mm in diameter before it was incident upon the samples. The resulting power density was ~91 mW/cm^2, which is within the safety limit.[71] Continuous ultrasonic waves were generated with a focused transducer (Ultran VHP100-1-R38), which had a 38-mm focal length and a 1-MHz central response frequency. Dimensions of the focal zone were ~20 mm along the ultrasonic axis and ~2 mm laterally. The peak pressures in the focal zone were ~10^5 Pa. A 12-bit CCD camera of 256×256 pixels (Dalsa CA-D1-0256T) was used to detect speckle patterns generated by scattered light transmitted through the sample. An iris was placed before the CCD camera to control the average speckle size on the CCD surface. In association with the adjustment of the iris aperture, the CCD exposure time was set to ensure that sufficient photons would be collected without decorrelation of speckle patterns. A computer was applied to control the CCD camera for implementing optical detection and for data transference. The computer also controlled a function generator that generated electrical signals, which were amplified by a power amplifier and then sent to drive the transducer. Speckle contrasts were measured under conditions with and without ultrasound modulation, and the differences in the speckle contrasts were taken as imaging signals, which were related to the ultrasound modulation depth.

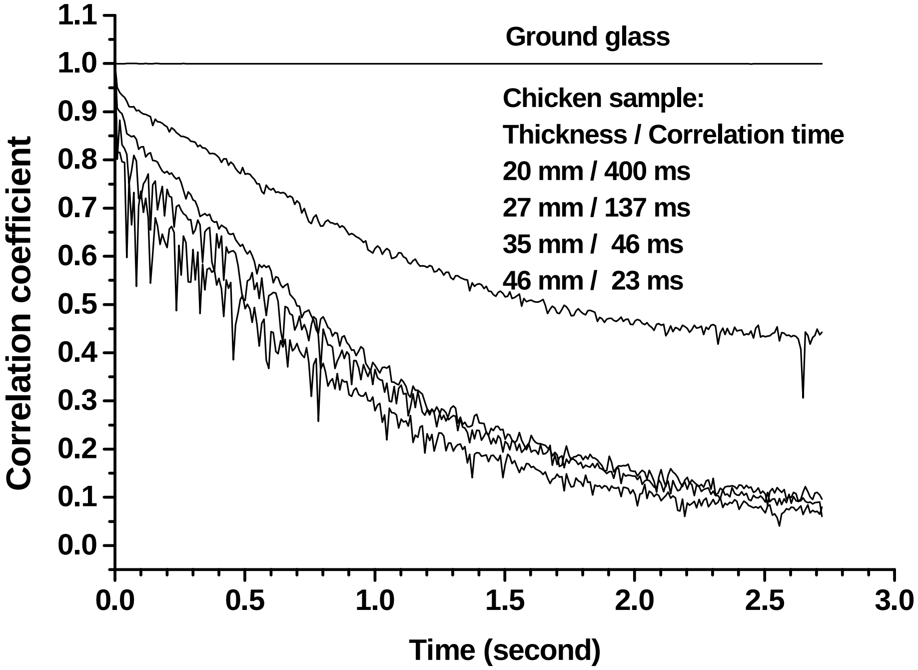

Fig. 21. Time-dependent correlation coefficients of speckle patterns generated with chicken breast tissues of various thicknesses. The result of ground-glass sample is shown for comparison.

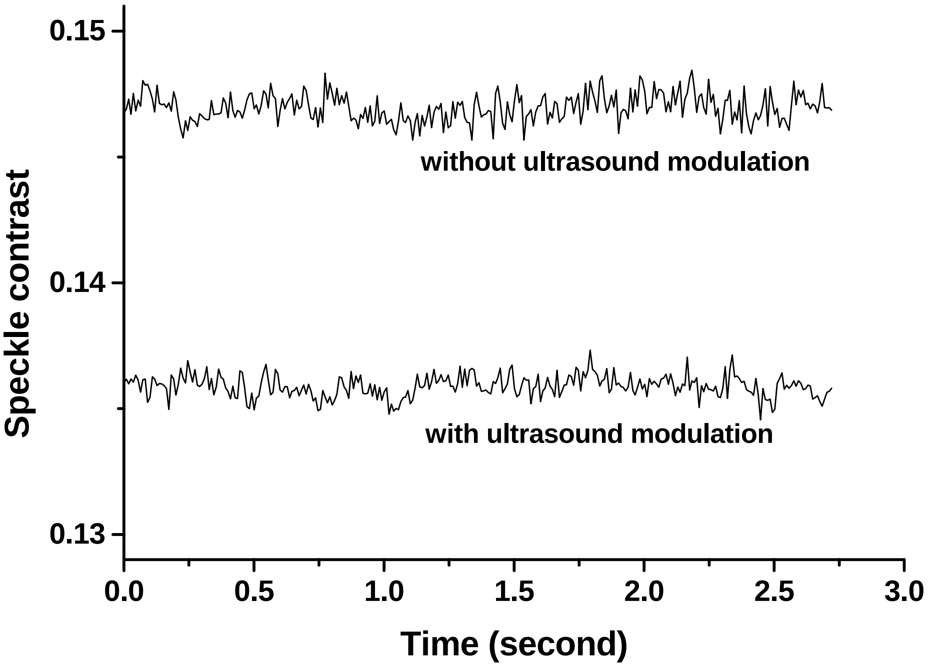

Fig. 22. Speckle contrasts *vs* time. The results of a 20-mm-thick chicken sample, which were obtained with and without ultrasound modulation, respectively, are compared.

3. Experimental results and discussion

Because biological tissues were used in our experiments, speckle noise, which is an intrinsic factor in tissue experiments, became a significant noise source in the signal detection. Movements of small particles inside biological tissue, e.g., Brownian motion, cause the noise, which leads to decorrelation of laser speckle patterns. To check the speckle pattern decorrelation, we measured correlation coefficients between speckle patterns within a time period of ~2.8 seconds (Fig. 21). Three hundred frames of speckle patterns were sequentially acquired with the CCD camera within the time period. The CCD exposure time was ~9 ms. Chicken-breast-tissue samples of various thicknesses were used. Because speckle pattern decorrelation is sensitive to movements of any of the components in the experimental setup, we did a measurement with a ground-glass sample first to check the setup. The result is presented in the figure. The correlation coefficient measured with the ground-glass sample did not change with time, maintaining a value of ~1, which indicated that the setup was stable enough for our purposes. The results from the chicken samples show that the correlation coefficients decrease rapidly as time elapses. Specifically, with the increase of sample thickness, the correlation coefficient decrease becomes more significant. Some spike-like fluctuations are seen in the curves, which are more remarkable in the thicker tissue experiments. By checking the experimental system and comparing the results with those from the ground-glass sample, we conclude that the fluctuations were caused by mechanical disturbances impacting the sample. The disturbance led to recoverable movements of photon scatters inside the tissue, which led to recoverable changes of the speckle patterns. Because it is soft, chicken tissue is more subject to mechanical disturbances, e.g., shape distortion, than the ground glass. Therefore, the fluctuation of the correlation coefficient was significant in the tissue samples. Since the photons had longer path lengths in thicker tissues, the influence of the disturbance was more significant and, as a consequence, the fluctuation was more remarkable in the thicker tissue samples. We define correlation time as the time period after which the correlation coefficient decreases from 1 to 0.8. The correlation time for the samples of thicknesses 20 mm, 27 mm, 35 mm, and 46 mm were found to be 400 ms, 137 ms, 46 ms, and 23 ms, respectively. The data imply that tomography of thick-biological-tissue samples using a CCD camera, which has a limited maximum frame rate, is challenging. The maximum frame rate of our CCD camera is ~200 frames/second. Because sufficient exposure is required, in practice the frame rate is usually lower. We had thought that speckle decorrelation would be much more significant in thick-biological-tissue experiments, and the data do, in fact, verify our suppositions. In parallel speckle detection, a four-frame acquisition or a two-frame acquisition is needed and the acquired frames must be correlated. For experiments using the detection, the sample thickness will be limited because of speckle decorrelation. We also expected that speckle-contrast detection would be efficient in thick-sample experiments, and we checked it experimentally in this chapter.

The speckle contrasts of the speckle patterns, which were studied in Fig. 21, were measured as functions of time. Measurements of samples with various thicknesses have similar results; there is no tendency indicating that speckle contrast varies with time although the speckle contrast does fluctuate in measurements taken at different moments. Figure 22 shows the results obtained with a 20-mm sample. With the increase of the sample thickness, the fluctuation becomes slightly significant. However, the fluctuation, which we define as the ratio of the standard deviation to the mean, increases very slowly with sample thickness. It is only ~1% in the case of a 46-mm sample. The speckle contrasts measured under ultrasound modulation for the 20-mm sample are also shown in the figure. Compared with the results obtained without ultrasound modulation, the only difference is that the speckle contrasts are lower under ultrasound modulation. It has been recognized that the variation in speckle contrast with ultrasound modulation is related to the ultrasound modulation depth, and it can, therefore, be used as an imaging signal. In the case of thick-sample imaging, the speckle-contrast measurement shows distinctive advantages; it needs only a one-frame acquisition to obtain speckle contrast, and an average can be done over multiple independent acquisitions to obtain a mean value.

Although the fluctuation of speckle contrast becomes somewhat significant for thick samples, sufficient SNRs for imaging can still be obtained by averaging the speckle contrasts, provided the ultrasound modulation depth is high enough.

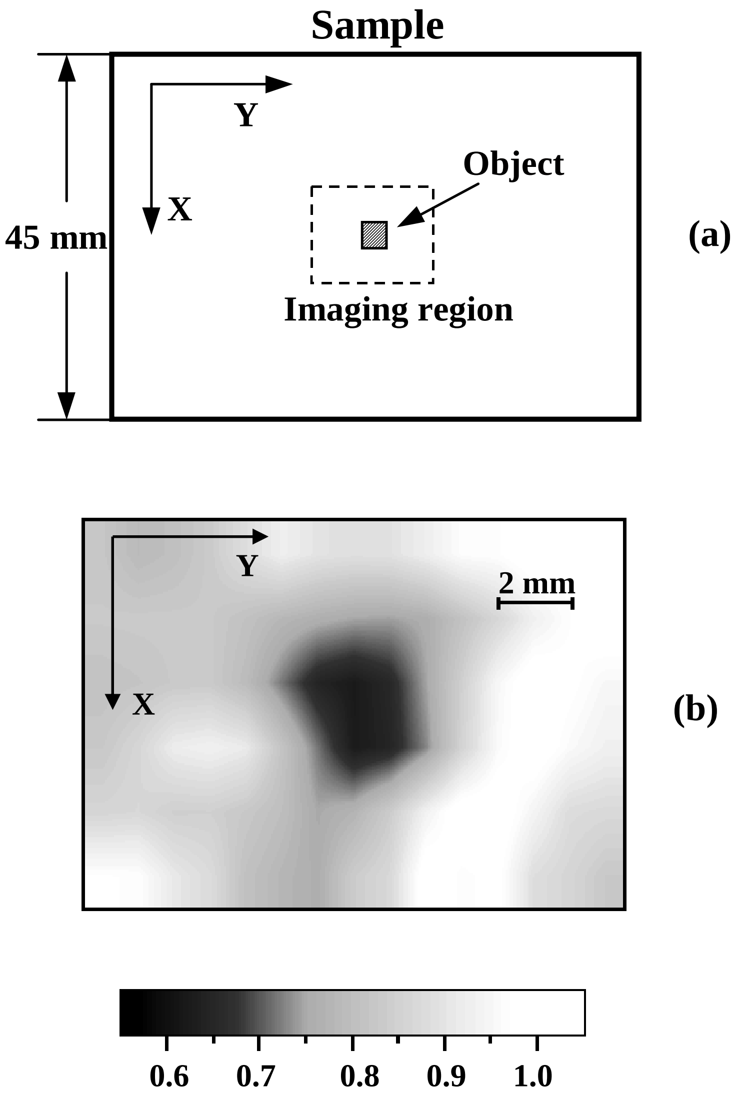

Fig. 23. (a) Sketch of a 45-mm-thick chicken-breast-tissue sample. An object is buried in the middle of the sample. The relative sizes of the object, imaging region and the whole sample are shown. (b) 2D image of the object. The image was obtained with the transmission-detection configuration.

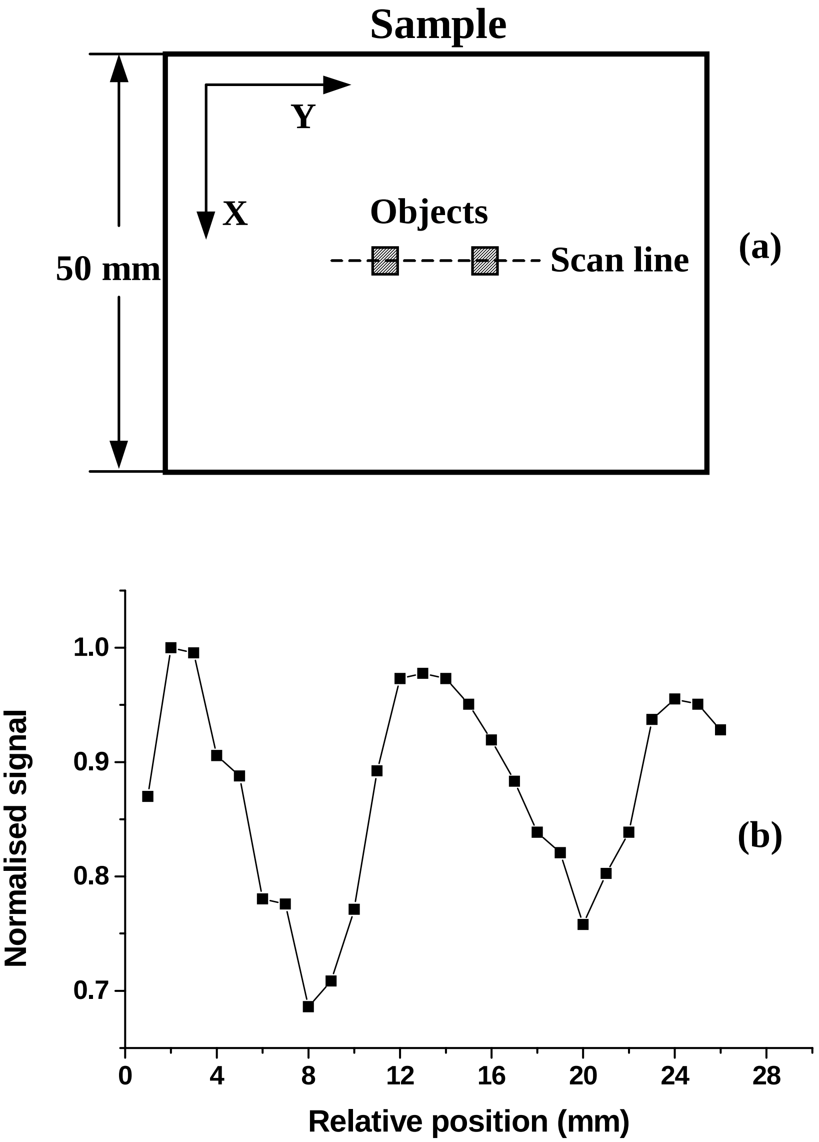

Fig. 24. (a) Sketch of a 50-mm-thick chicken-breast-tissue sample. Two objects are buried in the middle of the sample. (b) 1D image corresponding to the scan line indicated in (a), which is along the *Y* axis at the center of the sample. The image was obtained with the transmission-detection configuration.

By employing speckle-contrast detection, imaging experiments with thick-biological-tissue samples were carried out in a transmission-detection configuration. The tissue samples were made of chicken breast tissue, and the objects buried in the tissue were soft rubber, which had good acoustic coupling with the tissue and little acoustic absorption. The objects were buried in the middle plane of the sample. To obtain a 2D image, the transducer and the sample were scanned along the X and Y directions, respectively. At each scanning position, 200 measurements were made respectively with, and without, ultrasound modulation. The results were averaged. In this study, speckle-contrast detection[31] was improved, and efforts were made to monitor the SNRs and ensure that the detected signals had SNRs over unity. The mean and the standard deviation of the speckle contrasts obtained from each of the 200 measurements were checked for both cases — with and without ultrasound modulation. If the difference of the means (i.e., the imaging signal) was less than the sum of two standard deviations, which we defined as noise, the imaging signal was discarded and another 200 measurements were repeated until the signal was larger than the sum of the standard deviations, i.e, SNR > 1.

While applying the above rule for accepting or rejecting the imaging signal, images of thick samples with single, as well as double objects, were obtained. Figure 23(a) shows a sketch of a 45-mm-thick chicken sample, in which a buried object ($3.5 \times 3.1 \times 14.9\,\text{mm}^3$, along X, Y and Z directions, respectively), imaging region and the whole sample are drawn proportionally. Figure 23(b) shows a clear 2D image of the object. The SNRs in the measurement are ~3. Figure 24(a) shows a sketch of a 50-mm-thick chicken sample, in which two buried objects ($3.5 \times 3.1 \times 15.2$ mm^3 and

$3.3 \times 3.1 \times 15.2\,\text{mm}^3$, respectively) and the whole sample are drawn to scale and a scan line along the *Y* axis at the center of the sample is shown. Figure 24(b) shows a 1D image corresponding to the scan line indicated in Fig. 24(a). Two dips showing the objects are sharp in the figure. It should be noted that with such a thick sample, the image contrast is still quite good, up to ~30%. Also, the spatial resolution is approximately 2 mm, close to the size of the ultrasonic focal spot.

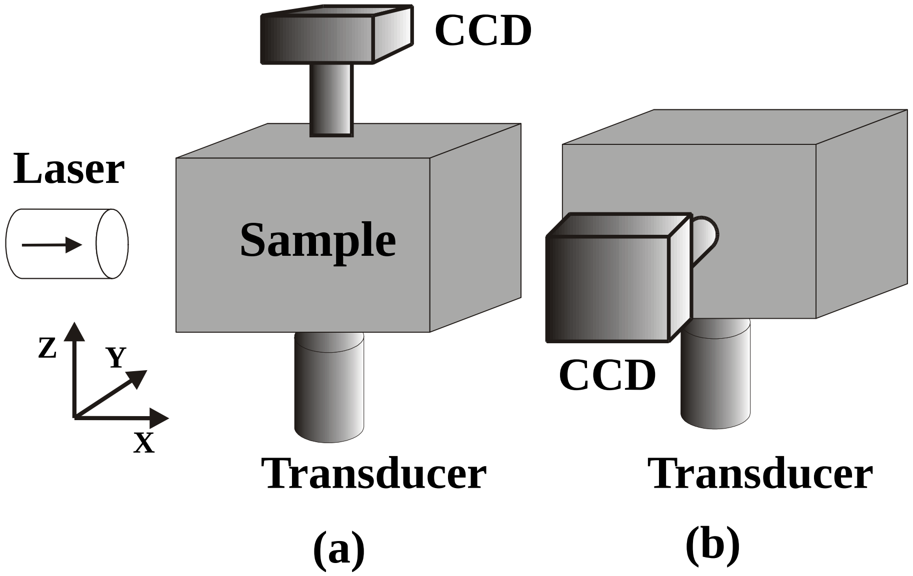

Fig. 25. Schematic of side-detection configurations. (a) The CCD camera and the transducer are located at two opposite sides of the sample; (b) The CCD camera is located at an angle of 90 degrees to the transducer.

In addition, we proposed a detection mode that we called side detection, which is an intermediate modality between the transmission and the reflection mode. Figure 25(a) and (b) show two configurations, respectively, in which the CCD camera and the transducer were placed at two opposite sides of the sample or the CCD was at an angle of

90 degrees to the transducer. The configuration in Fig. 25(a) was examined with an imaging experiment using a thick chicken sample ($40\times65\times50$ mm^3 along the X, Y and Z directions, respectively). An object of $3\times3\times13.8$ mm^3 was buried in the middle of the sample. To obtain a 2D image, the transducer was scanned along the X axis, and the sample was scanned along the Y axis, respectively. Figure 26(a) shows a 2D image of the buried object. The size of the object in the image agrees with the real size, and the image contrast is high (up to ~50%). In the configuration shown in Fig. 25(b), the incident laser, the CCD camera and the transducer were at an angle of 90 degrees to each other. The arrangement is more compact and convenient for application. The configuration was examined with an experiment that employed a chicken sample of $43\times65\times50$ mm^3. An object of $3.1\times3.0\times14.1$ mm^3 was buried 12 mm deep in the sample in the X direction. The transducer and the sample were scanned along the X axis and the Y axis, respectively. A clear image of the object was obtained, which is shown in Fig. 26(b). These results indicate that detection is nearly identical at any position around the sample because light is diffused after experiencing sufficient scattering in the thick-tissue samples. In Leveque *et al.*'s experiment using a reflection configuration,[33] they obtained an image with a significant shadow, which was inferior to the image obtained with the transmission configuration. Our results show that the images obtained in the side-detection configurations have similar qualities to those obtained in the transmission configuration. For application, side-detection is a more convenient configuration than transmission detection. Since the reflection configuration reported on so far placed the transducer at the side of sample, the side-detection configuration actually has the same convenience as reflection configuration. In addition, the strong surface reflection of light, which is

significant in the reflection mode, is avoided in side detection. This should lead to a higher SNR in side detection. In other words, side-detection configuration can be applied as an alternative to the reflection configuration.

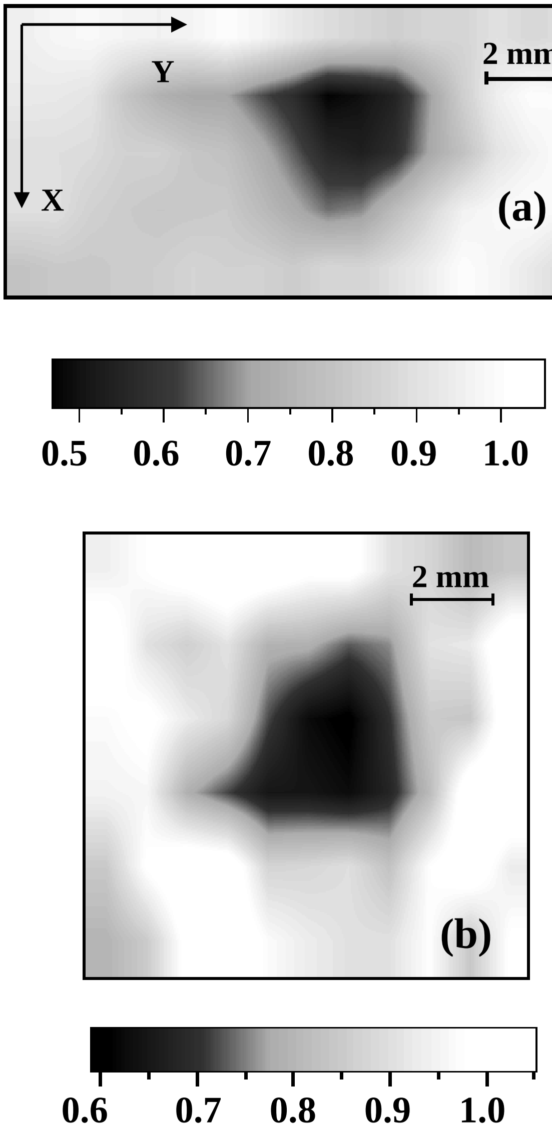

Fig. 26. 2D images obtained with side-detection configurations. (a) The image was obtained with the configuration shown in Fig. 25(a). The object was buried in the middle of a chicken-breast-tissue sample (size of $40 \times 65 \times 50$ mm^3). (b) The image was obtained with the configuration shown in Fig. 25(b). The object was buried 12 mm deep in the *X* direction in a chicken-breast-tissue sample (size of $43 \times 65 \times 50$ mm^3).

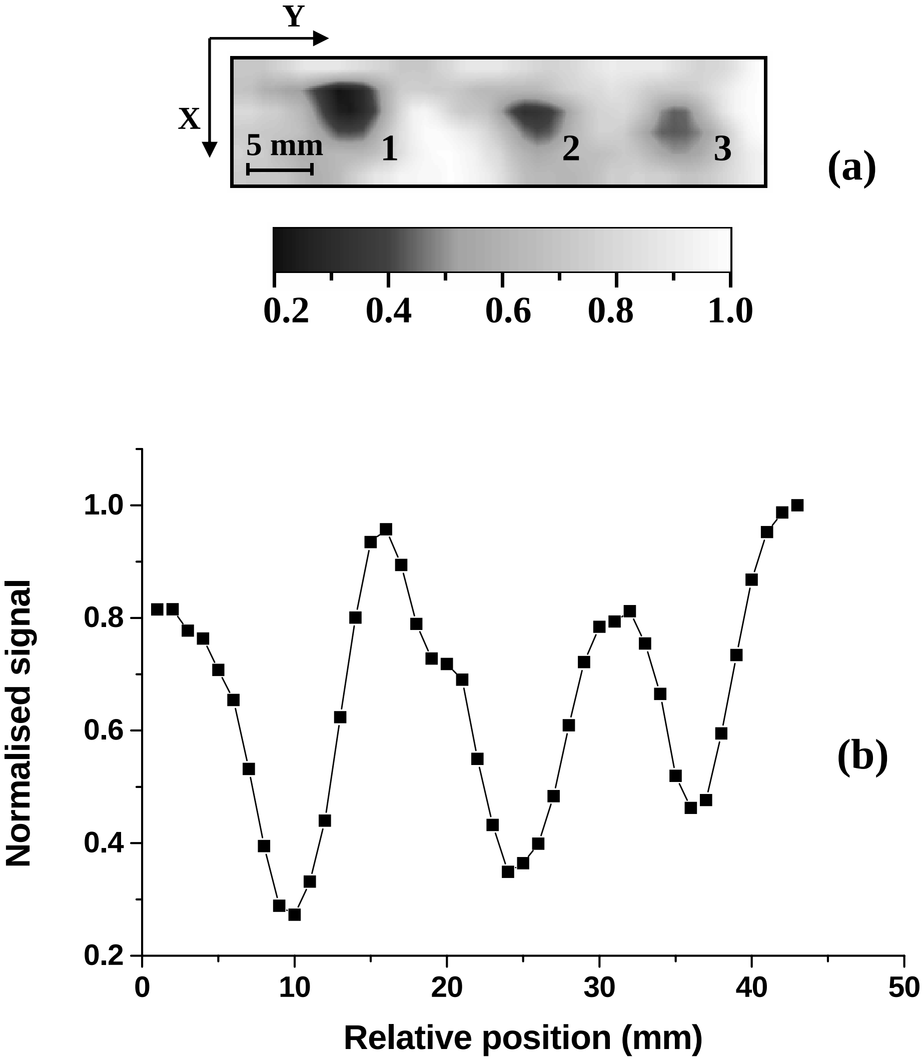

Fig. 27. (a) 2D image of three objects of different optical absorption: 1, black-surface object; 2, green-surface object; 3, (original) white-surface object. The image was obtained with the configuration shown in Fig. 25(a). (b) 1D image corresponding to a scan line across the objects along the *Y* axis.

With the side-detection configuration shown in Fig. 25(a), we tested the sensitivity of ultrasound-modulated optical tomography for identifying objects with different optical absorption properties. A chicken sample ($43 \times 65 \times 50$ mm^3, along the *X*, *Y* and *Z* directions, respectively) with three objects, which were buried in a plane 15 mm deep in the *X* direction, was used. The objects were soft white rubber, with identical sizes ($3 \times 3 \times 14$ mm^3). Surfaces of two of the objects were stained with black and green dyes, respectively, which led to differences in optical absorption between the objects; the black one had the strongest absorption and the one that was left (white) had the weakest absorption. A 2D image of the objects is shown in Fig. 27(a) and a 1D image corresponding to a scan line across the objects along the *Y* axis is shown in Fig. 27(b). The black, green and white objects are seen with different contrasts, which reflect the optical absorption correctly: the stronger the absorption, the higher the contrast. In detail, the contrast of the black one is ~12% and ~35% higher than that of the green one and the white one, respectively. It is seen that the differences in optical absorption from the objects' surfaces led to significant differences in image contrasts. This initial test shows that ultrasound-modulated optical tomography has good sensitivity for discriminating objects with different absorption properties.

Further, with the side-detection configuration, we measured the modulated signal, i.e., speckle-contrast difference along the *X* direction inside the tissue, which reflected photon density distribution. The measurement attempted to use the configuration to characterize the optical properties (absorption and scattering) of the biological-tissue samples. In this experiment, we used a diode laser (Melles Griot 56IMS667, wavelength: 690 nm; coherence length: over 1 m). For the measurements, the CCD camera and the transducer were kept fixed, and a thick chicken sample in a cubic shape ($47 \times 65 \times 50$ mm^3) was scanned along the *X* direction. According to diffusion theory, the photon fluence rate $\psi(x)$ deep inside a turbid medium decays exponentially with the distance *x* from the source, i.e., $\psi(x) \propto \exp(-\mu_{eff} x)$, where $\mu_{eff} \approx \sqrt{3\mu_a \mu_s'}$ is the effective attenuation coefficient, and μ_a and μ_s' are the absorption coefficient and the reduced scattering coefficient, respectively. By measuring the photon density distribution and fitting it with the above exponential function, one can obtain the effective attenuation coefficient.

Figure 28 shows a measured signal distribution. It is not smooth as expected; instead, the curve is composed of several segments. In each segment, the curve decays with the distance *x*. And at each interface between two segments, fluctuations occur. We repeated the measurement several times and obtained similar results. For comparison, we measured the signal distribution with a gelatin sample, which was uniform in structure and optical properties. The result showed a smooth decay curve without fluctuations. The chicken sample used in the experiment was made of chicken breast slices with different thicknesses. The measured signal fluctuations were found to be located at each interface between two slices. The signal fluctuations at the interfaces might be attributed to the presence of air bubbles between the slices, which could cause changes in acoustic impedance at the interfaces and induce signal fluctuations. We tried to fit the data of each segment in Fig. 28 with an exponential decay function and obtained effective attenuation coefficients of 0.799 cm^{-1} and 0.841 cm^{-1}, respectively, for the two segments, which agree with those reported by Marquez *et al.*.[72] According to Marquez *et al.*'s measurements, μ_a and μ_s' of chicken breast tissue at wavelength of 690 nm are ~0.1

cm^{-1} and ~2.2 cm^{-1}, respectively. The corresponding effective attenuation coefficient is 0.81 cm^{-1}. The results show that the optical properties (i.e., μ_{eff}) of different layers in the tissue sample could be determined individually by the measurement of ultrasound-modulated signals. Lev *et al.*[41] claimed successful application of this measurement in determining the optical properties of homogeneous turbid medium. Our experiment with a layer-structure tissue sample, together with the above sensitivity experiment, indicates that the ultrasound-modulation technique offers promise for the determination of spatially resolved optical properties in complicated inhomogeneous biological-tissue samples.

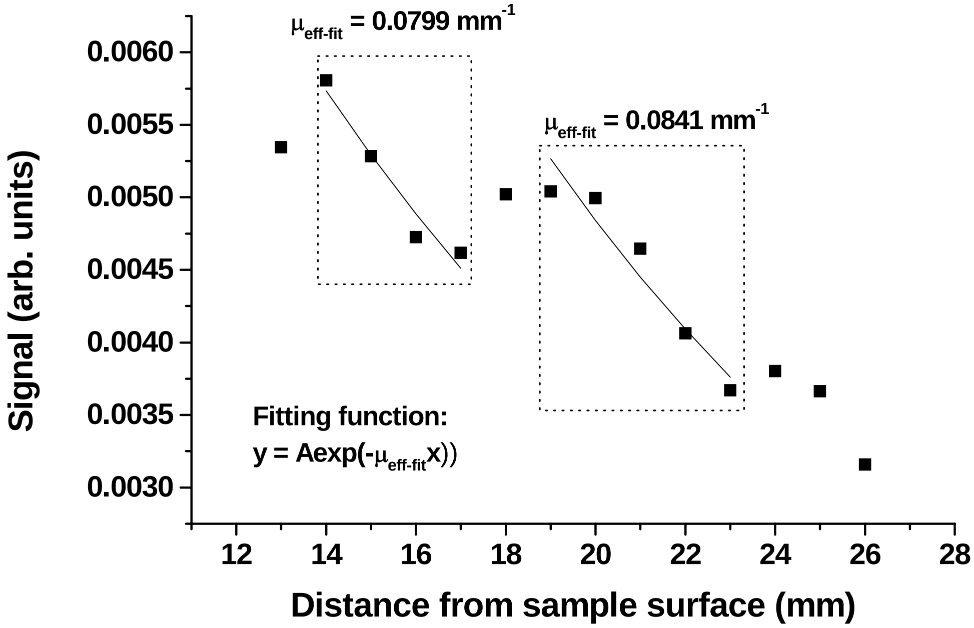

Fig. 28. Measured modulated signal distribution along the *X* direction inside a chicken-breast-tissue sample. Effective attenuation coefficients of the sample were deducted by fitting the data in each segment in the distribution with the 1D model of diffusion theory, respectively.

4. Summary

The ultrasound-modulated optical tomography of thick biological tissues was studied. Speckle decorrelation was investigated with samples of various thicknesses, and the speckle-contrast detection in thick-biological-tissue tomography was shown to have advantages over other techniques. With the resulting improved speckle contrast measurement, images of biological tissue samples of thicknesses up to 50 mm were successfully obtained in a transmission-detection configuration. This is the maximum thickness so far reported for ultrasound-modulated optical tomography. The image contrast was up to 30% and the image resolution was ~2 mm, which was determined by the ultrasonic focal spot size.

Side-detection configurations were proposed, which are more convenient than transmission configuration for practical applications and can be applied as alternatives to the reflection configuration. Experimental results showed that the images obtained with side-detection configurations had similar qualities to those obtained with transmission configuration, and they were far superior to images obtained with reflection-detection configuration. Further, two experiments were conducted with side-detection configuration to test the sensitivity of the ultrasound-modulated optical tomography for discriminating objects of different optical absorption and for measuring optical properties in a layer-structure sample, respectively. The results from these two experiments implied that the ultrasound-modulation technique is a promising one for characterizing the optical properties of complicated inhomogeneous tissue samples.

CHAPTER V

TOMOGRAPHY OF CROSS-SECTIONS CONTAINING ULTRASONIC AXIS

1. Introduction

In ultrasound-modulated optical tomography, by scanning a sample or an ultrasonic beam, 1D or 2D images of a cross-section perpendicular to the ultrasonic axis can be obtained directly. It is desirable that a three-dimensional (3D) image can be obtained. To obtain a 3D image, the cross-section containing the ultrasonic axis needs to be imaged. Usually, continuous-wave (CW) single-frequency ultrasounds are applied in the tomography. In these cases, image resolution is determined by the ultrasonic focal zone. Figure 29 shows amplitude distribution of an ultrasonic field. The brightest portion in the field corresponds to the ultrasonic focal zone, which is long in the axial direction and narrow in the lateral direction. Leveque-Fort[33] reported scanning an ultrasonic beam axially to image the cross-section containing the ultrasonic axis. The resolution of the image obtained in the experiment was poor because the axial dimension of the ultrasonic focal zone was quite long. Wang *et al.*[34] and Yao *et al.*[35] developed frequency-swept ultrasound-modulated optical tomography to improve the axial resolution and achieved controllable spatial resolution along the ultrasonic axis; this method was further studied recently by Forget *et al.*.[36] Another method which can provide good axial resolution is using pulsed ultrasound in the tomography, which has been studied by Hisaka *et al.*[37] and Lev *et al.*.[38] So far, no reconstruction algorithms have been employed in ultrasound-modulated optical tomography.

In the first part of this chapter, frequency-swept ultrasound-modulated optical tomography was studied experimentally to obtain high resolution (sub-millimeter resolution) imaging. In the second part, a novel imaging technique was developed, which is the first reconstruction-based technique for ultrasound-modulated optical tomography. We call it ultrasound-modulated optical computed tomography.

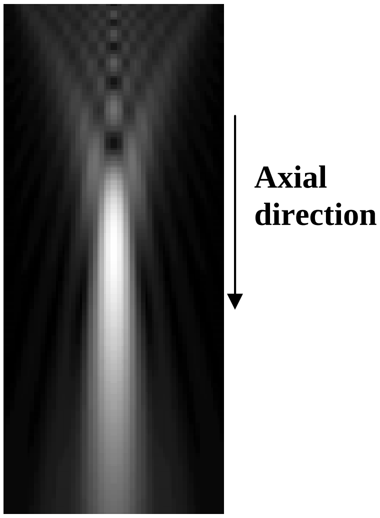

Fig. 29. Amplitude distribution of an ultrasonic field.

2. Frequency-swept ultrasound-modulated optical tomography

Frequency-swept ultrasound-modulated optical tomography with frequency sweep ranges of 3 MHz[34] or a few hundred kilohertz[35] had been studied. The image resolution in the axial direction in those experiments was half millimeter or a few millimeters. The purpose of present study is to examine that if the technique can be applied to obtain higher-resolution images in the ultrasonic axial direction by use of larger sweep ranges.

Objects smaller than 0.5 mm were embedded in scattering media and were expected to be imaged.

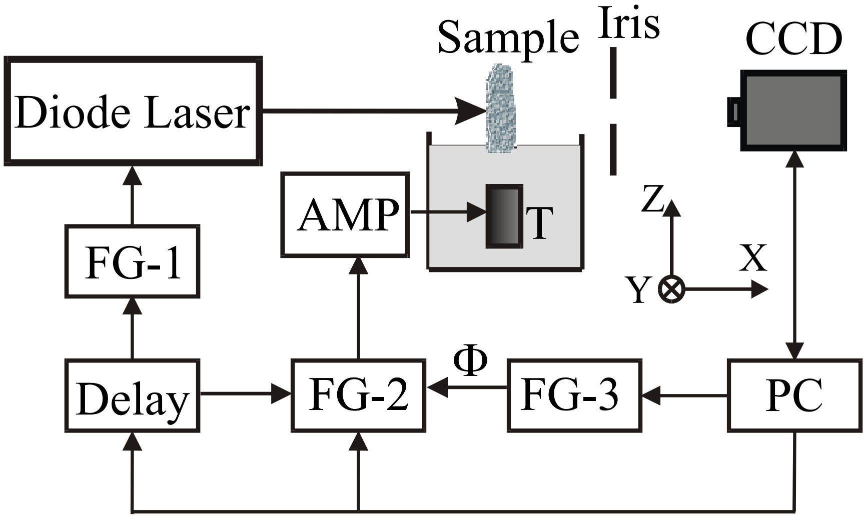

Fig. 30. Experimental setup: FG-1, FG-2, and FG-3, function generators; Delay, pulse-delay generator; AMP, rf amplifier; T, ultrasonic transducer; PC, computer.

2.1 Method

In the tomography, an ultrasonic transducer is driven by a frequency-sweep (it is also called chirp) function, which is a linear function of time. The instantaneous frequency of the frequency sweep is

$$f_u(t) = f_{u,0} + bt\,, \tag{44}$$

where $f_{u,0}$ is the starting frequency, b is the sweep rate, and t is the time. Along the ultrasonic axis, the instantaneous ultrasonic frequency at position z is

$$f_u(z,t) = f_{u,0} + b(t - \frac{z - z_0}{v_s}), \tag{45}$$

where z_0 is the coordinate of the initial position of the ultrasound at the transducer surface, and v_s is the speed of ultrasound in the medium. Light modulated by ultrasound at different positions in the ultrasonic column has different frequencies, which are expressed by the above equation. In the experiment, the laser beam is modulated with a frequency-sweep function similar to that of the ultrasound. The instantaneous frequency of the frequency sweep is

$$f_L(t) = f_{L,0} + b(t - \tau), \tag{46}$$

where $f_{L,0}$ is the starting frequency, and τ is the time delay between the sweeps of the ultrasound and the laser. The frequency of the heterodyned signal is

$$f_h(z,\tau) = \left| f_{u,0} - f_{L,0} + b(\tau - \frac{z - z_0}{v_s}) \right|, \tag{47}$$

which is dependent on the position z and independent of time. So, by detecting the heterodyned signals of different frequencies, one can obtain an image reflecting optical properties at different locations along the ultrasonic axis inside the ultrasonic column.

2.2 Experimental setup

The signal-detection method used here was similar to that used in Yao *et al.*'s study.[35] The experimental system was improved in the present experiment.

Figure 30 shows the experimental setup. The diode laser, CCD camera, function generators, and rf power amplifier were the same devices that were used in the experiments in previous chapters. A focused ultrasonic transducer (Imasonic, 3800A101) with a 6-mm focal length in water and a 15-MHz central frequency was used. The –6 dB bandwidth of the transducer was ~7 MHz. The ultrasonic focal spot size was ~0.1 mm. In frequency-swept ultrasound-modulated optical tomography, spatial resolution Δz along the ultrasonic axis is determined by the sweep range Δf : $\Delta z \approx v_s / \Delta f$.[35] In the experiment, the frequency-sweep range was set as 7 MHz, which would lead to image resolution of ~0.2 mm. Three function generators (FG-1, FG-2, and FG-3) were used, which shared the same time base to ensure synchronization. FG-1 and FG-2 sent frequency-sweep sinusoidal waves to modulate the laser and drive the transducer, respectively. A pulse-delay generator sent trigger signals to FG-1 and FG-2, which had a time delay τ between each other. To extract the heterodyned signal, we applied FG-3 to generate a sinusoidal wave with the same frequency as the heterodyned signal, which was sent to modulate the amplitude of the output of FG-2. Four sequential acquisitions with the sinusoidal wave having an initial phase of 0, 90, 180, and 270 degrees respectively were taken to implement parallel lock-in detection. The CCD camera, the pulse-delay generator, FG-2, and FG-3 were controlled with a computer. The computer controlled the amplitude of the signal output from FG-2, the initial phase of the signal output from FG-3, and the time delay set on the pulse-delay generator.

2.3 Experimental studies

Firstly an experiment was done with a 1-MHz transducer and a frequency-sweep range of 400 kHz to test the system in a tissue-phantom sample. For the frequency-sweep range, expected image resolution was ~3.8 mm. Tissue-phantom samples used in the experiments were made from a mixture of gelatin and intralipid solution, which had a reduced scattering coefficient of ~3 cm^{-1}, similar to that of chicken tissue. An object made of soft rubber with a size of ~3.3 mm in the direction of the ultrasonic axis was buried at a depth of ~7 mm below the sample surface. As expected, the object was resolved in images.

Then experiments were carried out with the 15-MHz transducer to image objects smaller than half millimeter. Tissue phantom samples as well as chicken tissue samples were used. A piece of black hair of ~0.2 mm in diameter was buried as an absorbent object at depths of 1.5-2 mm below a sample surface in both X and Z directions. The CCD camera was placed off the optical axis to collect diffuse light, and the step size of the electronic scan along the Z axis was 60 microns. In the experiments, the laser beam was focused at the imaging layer to enhance the signal. However, the signal-to-noise ratios were not good enough, which were just above unity. Images obtained were not good. The low signal-to-noise ratios were attributed to the fact that the spatial volume contributed to the signal was very small, which was approximately in a cylindrical shape of ~0.2 mm in length and ~0.1 mm in diameter.

2.4 Summary

The frequency-sweep technique was studied for high resolution imaging by applying a 7-MHz frequency-sweep range. The preliminary experiments indicated that there was a tradeoff between the resolution and the imaging signal. Because the volume contributed to the signal is small in the case of high-resolution imaging, the signal is weak. To obtain good images with high resolution, efforts need to be made to improve the signal-to-noise ratio. Raising the ultrasonic intensity can raise the signal. This can be done by using an ultrasonic transducer with high efficiency, or raising the input electrical power of a transducer. Because of the tradeoff between the efficiency and the bandwidth of a transducer, the efficiency of a broad bandwidth transducer used in frequency-swept optical tomography will not be high enough. On the other side, to raise the ultrasonic intensity by raising the input electrical power of a transducer, one should be careful with the damage threshold of the transducer. A transducer may be damaged by thermal effects if the average input electrical power is over a certain level. Running a transducer in burst mode instead of CW mode may overcome this restriction.

3. Ultrasound-modulated optical computed tomography (UMOCT)*

UMOCT was developed with inspiration from X-ray computed tomography (CT). In X-ray CT, through multiple linear and angular scans around a sample carried out with an X-ray source-detector pair, a cross-sectional image of the sample is reconstructed from the detected X-ray intensities, which reflect the attenuation properties along the X-ray paths in the sample. In ultrasound-modulated optical tomography, ultrasound-modulated optical signals are generated in the volume that is occupied by the ultrasonic beam in the sample. Intensities of the ultrasound-modulated optical signals reflect the optical properties (optical absorption and scattering) in this volume. Motivated by the analogy with X-ray CT, I developed the UMOCT in which a filtered back-projection algorithm was applied

---

* Reprinted with permission from J. Li and L.-H. V. Wang, "Ultrasound-modulated optical computed tomography of biological tissues," Appl. Phys. Lett. **84**, 1597-1599 (2004). Copyright 2004 American Institute of Physics. The URL is: http://link.aip.org/link/?apl/84/1597.

to reconstruct images of cross-sections formed by the scanned ultrasonic axis. It should be noted that, in UMOCT, the scanning beam was an ultrasonic beam, and the signals to be detected were optical signals.

3.1 Method

Figure 31(a) shows a schematic of the experimental setup. Any signal-detection schemes used in conventional ultrasound-modulated optical tomography, such as detections with a single detector or multiple detectors (i.e., parallel speckle detection or speckle contrast detection), can be employed in UMOCT. In this study, I adopted the parallel speckle detection scheme. The hardware and the extraction of ultrasound-modulated signals were similar to those described before.

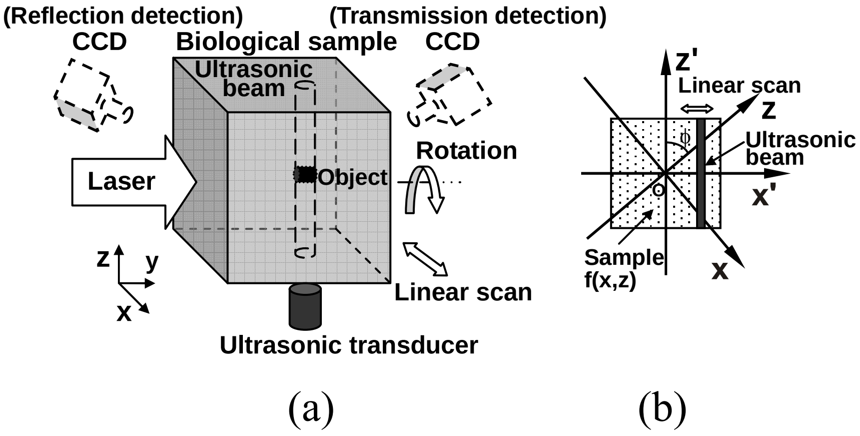

Fig. 31. Schematics of (a) the experimental configuration and (b) a cross-section of a sample with coordinates considered in the reconstruction.

In Fig. 31(a), a laboratory coordinate system is shown to describe the sample in its original orientation. The optical axis was along the *y* axis, and the ultrasonic axis was along the *z* axis. A laser beam of 690 nm in wavelength and 11 mW in power from a diode laser (Melles Griot, 56IMS667) was expanded to 20 mm in diameter to illuminate the sample perpendicularly. The coherence length of the laser was ~6 cm when it was modulated at 1 MHz. Ultrasonic waves, generated by a focused ultrasonic transducer (UltranLab, VHP100-1-R38) with a 38-mm focal length in water and a 1-MHz central response frequency, were coupled into the tissue sample through water in which the sample was partially immersed. The focal zone of the ultrasonic waves was 2 mm in diameter and 20 mm in length, in which the peak pressure was $\sim 10^5$ Pa. Speckle patterns generated by the scattered light from the tissue were detected by a 12-bit digital CCD camera (Dalsa, CA-D1-0256T) with 256×256 pixels. Then, ultrasound-modulated optical signals were extracted from the speckle patterns.

Experiments with a transmission-detection configuration, in which the CCD camera and the incident laser beam were on opposite sides of the sample, as well experiments with a reflection-detection configuration, in which the CCD camera and the incident laser beam were on the same side of the sample, were carried out. The UMOCT required relative linear and angular scans between the sample and the ultrasound. In the experiments, the position of the ultrasonic transducer was fixed. A sample holder was made to allow the sample to be rotated around the *y* axis by a rotational stage and to be linearly scanned along the *x* axis by a stepper motor. Figure 31(b) shows a cross-section of the sample on the *xz* plane, which has been rotated around the *y* axis by an angle ϕ from its original orientation. A new coordinate system ($x'y'z'$) is set with the z' axis parallel to the ultrasonic beam. In the figure, the ultrasonic beam is located at a distance x' from the origin.

The detected ultrasound-modulated optical signal can be expressed as an integration of the signal coming from each segment along the z' axis $(z'-\delta z'/2, z'+\delta z'/2)$ in the ultrasonic column:

$$s(\phi, x') = \int s_{\phi,x'}(z')dz', \tag{48}$$

which is a Radon transform. The integrand can be expressed as $s_{\phi,x'}(z') = C_1 Q_{\phi,x'}(z') m_{\phi,x'}(z') G_{\phi,x'}(z')$, where C_1 is a constant; $Q_{\phi,x'}(z')$ represents the photon density in the segment centered at z', determined by the photon transport from the laser source to this segment; $m_{\phi,x'}(z')$ is the depth of ultrasonic modulation related to the optical properties at z' in the ultrasonic column; and $G_{\phi,x'}(z')$ represents the Green's function describing the transport of the ultrasound-modulated photons from this segment to the detector. In the diffusion regime, $Q_{\phi,x'}(z')$ and $G_{\phi,x'}(z')$ have a weak dependence on z'.

The signals detected at multiple projection angles are used as the projection data for the reconstruction of an image reflecting the optical properties of the sample, where a filtered back-projection algorithm is applied. The Fourier transform of the signal $s(\phi, x')$ is defined as

$$S(\phi, \omega) = \int_{-\infty}^{\infty} s(\phi, x') \exp(-i\omega x')dx', \tag{49}$$

where ω is the spatial frequency in the x' direction. The filtered back-projection was implemented with the following process: (a) filtering $S(\phi,\omega)$ with a Ram-Lak filter $|\omega|$, (b) inverse Fourier transforming the filtered signal, and (c) summing the result. An offset was applied to the result to cancel out the negative values generated in the filtering process. The reconstructed image of the sample is expressed as

$$\hat{f}(x, z) = \int_0^{\pi} \int_{-\infty}^{\infty} S(\phi, \omega)|\omega| \exp(i\omega x')d\omega d\phi \,. \tag{50}$$

The reconstructed values represent the relative intensities of the ultrasound-modulated optical signals. The lower intensities reflect higher attenuation in the sample and vice versa.

3.2 Results and Discussion

In the experiment, the step size of the linear scan along the *x'* axis was 1.2 mm, and the increment of the angular scan was 5^{o}. To avoid the influence of acoustic heterogeneity on the ultrasound-modulated optical signal, all-biological-tissue samples were used: optically absorbent objects buried in background biological tissue were also biological tissues. Both the objects and the background tissue had similar acoustic impedance. The technique was first examined in the transmission-detection configuration. To ensure that the experiment involved only diffuse light, the CCD camera was placed at an angle of 25^{o} with respect to the optical axis to eliminate any contribution from ballistic photons. Figure 32(a) shows a photograph of a cross-section of a chicken-breast-tissue sample on the *xz* plane. A piece of chicken blood vessel, which had a size of ~8×3 mm^2 on the *xz* plane and ~2 mm in the *y* direction, was buried in the middle of a 14-mm-thick sample. Figure 32(b) shows the reconstructed image, in which the buried object is clearly seen. The size and the orientation of the object in the image are in good agreement with the actual ones.

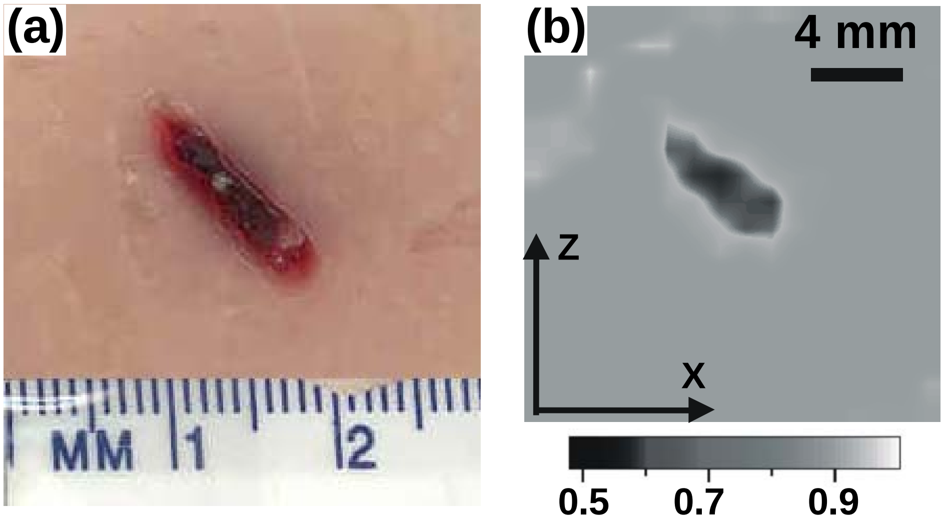

Fig. 32. Experimental result in the transmission-detection configuration. (a) Photograph of a cross-section on the *xz* plane located in the middle of a 14-mm-thick chicken-breast-tissue sample, in which an object made from blood vessel was buried. (b) Reconstructed 2D image.

The technique was also examined in the reflection-detection configuration. A chicken-breast-tissue sample was used, in which an object made from turkey muscle was buried ~9 mm deep in the *y* direction. The size of the object on the *xz* plane was ~4×3 mm^2. Figure 33(a) shows a photograph of the imaged cross-section of the sample, and Figure 33(b) shows the reconstructed image. The object is clearly visible in the image and its size matches the actual size quite well. 1D images across the center of the object along the *x* and *z* axes, respectively, are shown in Fig. 33(c). The resolution in both of the directions was ~2 mm, which shows that the resolution in UMOCT is determined by the diameter of the ultrasonic focal zone (2 mm).

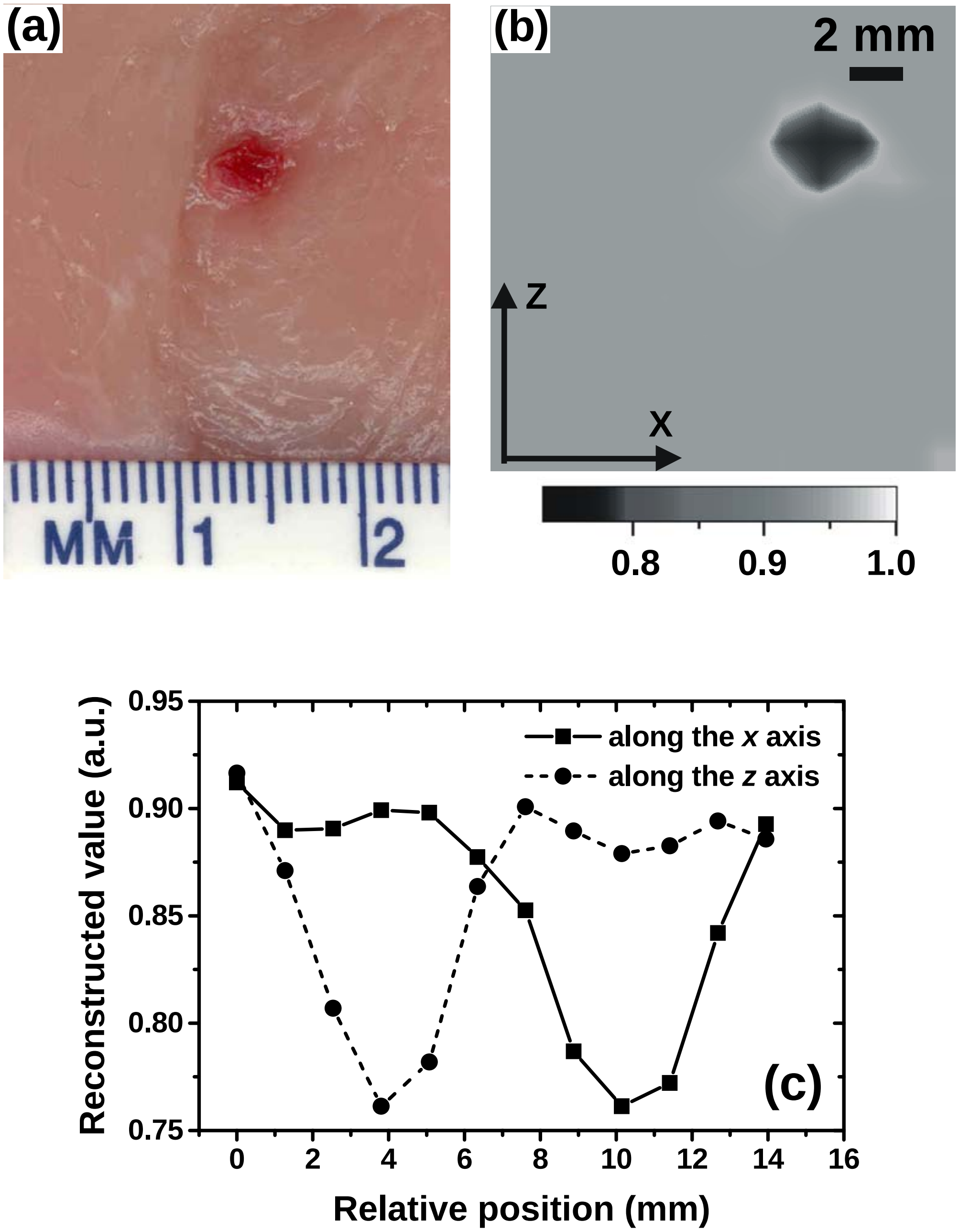

Fig. 33. Experimental result in the reflection-detection configuration. (a) Photograph of a cross-section on the *xz* plane located ~9 mm deep in a chicken-breast-tissue sample, in which an object made from turkey muscle was buried. (b) Reconstructed 2D image. (c) 1D images across the center of the object in (b) along the *x* axis and *z* axis, respectively.

As demonstrated in conventional ultrasound-modulated optical tomography, the resolution in the *y* dimension is determined by the diameter of the ultrasonic focal zone as well. A better resolution can be obtained through the use of an ultrasonic transducer with a focal zone of smaller diameter, e.g., 0.4 mm, which can be achieved by a 5-MHz transducer with the same geometry as the 1-MHz transducer used in the experiment. In this case, the resolution will be improved to ~0.4 mm whereas the imaging area will be smaller because of the shortened focal zone.

The reflection detection configuration is desired for medical imaging because of its convenient configuration. The results here demonstrate the latest progress in ultrasound-modulated optical tomography. Biological tissues are imaged for the first time in the reflection detection configuration and cross-sectional images are obtained also for the first time in this configuration, which allows three-dimensional tomography with good image resolution to be attainable. The results imply that the technique using the reflection detection configuration has good potential for application in medical imaging. In applications such as brain imaging, the incident laser beam and the detector will be located on the top of the head of a human being or an animal, and the ultrasonic transducer will be scanned around the head. It is expected that two-dimensional optical cross-sectional images as well as three-dimensional images at various depths in the brain, which have a controllable image resolution determined by the ultrasonic beam, can be obtained non-invasively with this technique.

In the experiments, data were acquired and calculated with a Pentium 200-MHz-CPU computer, and the rotation of the sample was implemented by hand. A measurement with 36 project angles took ~3 hours using the present system. Using a faster computer and rotating the sample with a motor-driven rotation stage will improve the data acquisition speed. The power density of the incident laser beam can be raised from the present ~3.5 mW/cm^2 to the safety limit of ~200 mW/cm^2 to greatly reduce the CCD exposure time and, consequently, the acquisition time. With these improvements, the data acquisition will be completed in minutes. The acquisition speed can be further improved in the future by the use of an ultrasonic transducer array and parallel implementations.

This technique is shown to be another effective tool, in addition to frequency-swept ultrasound-modulated optical tomography, for obtaining spatial resolution along the ultrasonic axis. In frequency-swept ultrasound-modulated optical tomography, the axial resolution is determined by the frequency span of the chirp function. It has been recognized that there is a tradeoff between the resolution and the signal intensity. And in that technique, an ultrasonic transducer with a broad bandwidth is required, which may not be efficient for ultrasonic modulation because of the tradeoff between transducer efficiency and bandwidth. In comparison, the resolution in UMOCT is determined by the diameter of the ultrasonic focal zone. A fine resolution can be achieved with sufficient signal intensities using a narrow-band high-efficiency ultrasonic transducer.

The method of X-ray CT has been applied in the optical regime for several years.[73–75] These applications have however been limited to ballistic-photon detection, i.e., ballistic imaging. The experiments here show that UMOCT extends the application of the method of X-ray CT to diffuse-light imaging with the aid of ultrasonic modulation.

3.3 Summary

A technique called ultrasound-modulated optical computed tomography was developed and its feasibility was proved experimentally in biological tissues in both optical transmission- and reflection-detection configurations. Clear 2D images of biological tissues in cross-sections containing the scanned ultrasonic axis were obtained with a resolution of 2 mm, which was determined by the diameter of the ultrasonic focal zone. The technique can be implemented with any standard signal-detection scheme for ultrasonic modulation of coherent light in scattering media and can be applied directly to achieve three-dimensional images of biological tissues.

CHAPTER VI

CONCLUSION

In this dissertation, ultrasound-modulated optical tomography was studied experimentally. The study was focused primarily on four aspects.

In ultrasound-modulated optical tomography, a laser source of long coherence length is necessary because ultrasonic modulation is primarily based on the mechanism of phase modulation. Laser speckles are thus common phenomena in the tomography, which are generated by scattered light transmitted through turbid media such as biological tissues. As optical polarization provides a unique contrast mechanism in optical imaging, it can be utilized in ultrasound-modulated optical tomography. The polarization properties of laser speckles generated from turbid media was investigated. A detailed study of degree of polarization in laser speckle fields was implemented. The knowledge obtained in the study is important for understanding the polarization phenomenon in turbid media including biological tissues and is helpful to applications of polarization in biomedical optics.

In ultrasound-modulated optical tomography, ultrasound-modulated signal is generated in a small volume occupied by the focused ultrasonic beam inside a biological tissue. The signal is buried in a huge background of un-modulated scattered light. To extract the weak signal, several signal-detection schemes were investigated. One of the detection schemes was based on optical filtering with a Fabry-Perot interferometer, which played as an optical filter. Preliminary experiments show that by use of the interferometer, the affect of the background can be greatly reduced and the technique is promising in applications of tomography with high-frequency ultrasound, i.e., high-resolution tomography. As a multiple-detector detection scheme, parallel-lock-in detection was studied. Multiple signal-acquisition methods were developed to improve the parallel-lock-in detection, which were proved with experiments to be superior to the conventional detection method. With these methods, the influence of the speckle-pattern decorrelation could be reduced and the signal-acquisition speed could be doubled. Biological-tissue samples were successfully imaged with expected resolutions. In addition, a novel signal-detection scheme was developed for ultrasound-modulated optical tomography, which was based on speckle-contrast measurement. The properties of laser speckles generated from biological tissues, in which ultrasonic modulation was applied, was investigated. Ultrasound-modulated optical tomography based on this signal-detection scheme, which combines speckle-contrast measurement with ultrasonic modulation, was found superior to the conventional speckle-contrast-based purely optical imaging because it provided better image resolutions. And, it was found superior to the parallel lock-in detection as it provided better image contrasts.

Tomography of thick-biological-tissue samples was studied. Experiments showed that when the sample thickness was increased, the speckle-pattern decorrelation became more significant and its influence on the signal detection became more serious. This fact seemed to be likely to preclude parallel-lock-in detection based ultrasound-modulated optical tomography from applying to thick-biological-tissue imaging. Experiments with samples of various thicknesses showed that speckle contrast was less affected by the speckle-pattern decorrelation and speckle-contrast detection scheme was efficient for thick-tissue imaging. With the speckle-contrast detection, images of biological-tissue samples of thicknesses up to 50 mm were obtained with good resolutions of ~2 mm, which is the maximum thickness so far reached with ultrasound-modulated optical tomography. This important result demonstrates that ultrasound-modulated optical tomography is promising for medical imaging such as breast-tissue imaging. In addition, detection configurations including transmission detection configuration and side-detection configuration were studied with thick-tissue imaging experiments.

To develop ultrasound-modulated optical tomography for three-dimensional imaging, techniques for imaging cross-sections containing ultrasonic axis were studied. In the study, two techniques were investigated for obtaining images of the cross sections: frequency-swept ultrasound-modulated optical tomography and ultrasound-modulated optical computed tomography. Frequency-swept ultrasound-modulated optical tomography was studied for sub-millimeter resolution imaging, in which high-frequency ultrasound and broad frequency sweep ranges were applied. Experiments indicated that efforts were needed to improve the signal-to-noise ratio in the high-resolution imaging in order to obtain images of good quality. A novel technique — ultrasound-modulated optical computed tomography was developed, in which an image reconstruction method was applied to reconstruct images of the cross-sections. It is the first image reconstruction method that is developed for ultrasound-modulated optical tomography. The technique was successfully applied in a reflection-detection configuration. Experiments demonstrated that it was feasible to obtain three-dimensional images of good resolutions by the use of ultrasound-modulated optical tomography in practical applications.

In summary, in the dissertation, studies were carried out to develop ultrasound-modulated optical tomography to be an efficient imaging tool for biomedical diagnosis.

Techniques with regard to signal detection and image reconstruction were explored. The results show that ultrasound-modulated optical tomography holds the promise for biomedical applications. Ultrasound-modulated optical tomography is however a developing image modality in the biomedical field, which is still at the early stage of the development. Further studies in-depth are expected. It is expected that ultrasound-modulated optical tomography will be applied to image living tissue in the near future, with further developments of signal detection schemes, e.g., implementation of fast acquisition with good signal-to-noise ratios.

REFERENCES

1. R. R. Alfano and J. G. Fujimoto, eds., Advances in Optical Imaging and Photon Migration, Vol. 2 of Topics in Optics and Photonics Series (Optical Society of America, Washington, D.C., 1996).
2. W. F. Cheong, S. A. Prahl, and A. A. J. Welch, "A review of the optical properties of biological tissues," IEEE J. Quantum Electronics **26**, 2166-2185 (1990).
3. V. G. Peters, D. R. Wyman, M. S. Patterson, and A. G. L. Frank, "Optical properties of normal and diseased human breast tissues in the visible and near infrared," Phys. Med. Biol. **35**, 1317-1334 (1990).
4. T. L. Troy, D. L. Page, and E. M. Sevick-Muraca, "Optical properties of normal and diseased breast tissues: prognosis for optical mammography," J. Biomed. Optics **1**, 342-355 (1996).
5. J. R. Mourant, A. H. Hielcher, A. A. Eick, T. M. Johnson, and J. P. Freyer, "Evidence of intrinsic differences in the light scattering properties of tumorigenic and nontumorigenic cells," Cancer **84**, 366-374 (1998).
6. A. Santinelli, M. Baccarini, P. Colanzi, and G. Fabris, "Microvessel quantitation in intraductal and early invasive breast carcinomas," Anal. Quant. Cyt. Hist. **22**, 277-284 (2000).
7. J. C. Hebden and D. T. Delpy, "Enhanced time-resolved imaging with a diffusion model of photon transport," Opt. Lett. **9**, 311-313 (1994).
8. B. Das, K. Yoo, and R. R. Alfano, "Ultrafast time gated imaging," Opt. Lett. **18**, 1092-1094 (1993).

9. S. Marengo, C. Pepin, T. Goulet, and D. Houde, “Time-gated transillumination of objects in highly scattering media using a subpicosecond optical amplifier,” IEEE J. Sel. Top. Quant. **5**, 895-901 (1999).
10. A. F. Fercher, “Optical coherence tomography,” J. Biomed. Opt. **1**, 157-173 (1996).
11. G. Yao and L.-H. Wang, “Two-dimensional depth-resolved Mueller matrix characterization of biological tissue by optical coherence tomography,” Opt. Lett. **24**, 537-539 (1999).
12. M. A. O’Leary, D. A. Boas, B. Chance, and A. G. Yodh, “ Experimental images of heterogeneous turbid media by frequency domain diffusing-photon tomography,” Opt. Lett. **20**, 426-428 (1995).
13. S. B. Colak, D. G. Papaioannou, G. W. t Hooft, M. B. van der Mark, H. Schomberg, J. C. J. Paasschens, J. B. M. Melissen, and N. A. A. J. van Asten, “Tomographic image reconstruction from optical projections in light-diffusing media,” Appl. Opt. **36**, 180-213 (1997).
14. R. A. Kruger and P. Liu, “Photoacoustic ultrasound: theory,” in *Laser-Tissue Interaction V*, S. L. Jacques, ed., Proc. SPIE **2134A**, 114-118 (1994).
15. A. A. Oraevsky, R. O. Esenaliev, S. L. Jacques, and F. K. Tittle, “Laser optic-acoustic tomography for medical diagnostics: principles,” in *Biomedical Sensing, Imaging, and Tracking Technologies I*, R. A. Lieberman, H. Podbielska, and T. Vo-Dinh, eds., Proc. SPIE **2676**, 22-31 (1996).
16. C. G. A. Hoelen, F. F. M. de Mul, R. Pongers, and A. Dekker, “Three-dimensional photoacoustic imaging of blood vessels in tissue,” Opt. Lett. **23**, 648-650 (1998).

17. L.-H. Wang and Q. Shen, "Sonoluminescence tomography of turbid media," Opt. Lett. **23**, 561-563 (1998).

18. G. D. Mahan, W. E. Engler, J. J. Tiemann, and E. Uzgiris, "Ultrasonic tagging of light: theory," Proc. Natl. Acad. Sci. USA **95**, 14015-14019 (1998).

19. W. Leutz and G. Maret, "Ultrasonic modulation of multiply scattered light," Phys. B **204**, 14-19 (1995).

20. L.-H. V. Wang, "Mechanisms of ultrasonic modulation of multiply scattered coherent light: an analytic model," Phys. Rev. Lett. **87**, (043903) 1-4 (2001)

21. L.-H. V. Wang, "Mechanisms of ultrasonic modulation of multiply scattered coherent light: a Monte Carlo model," Opt. Lett. **26**, 1191-1193 (2001).

22. S. Sakadžić and L.-H. V. Wang, "Ultrasonic modulation of multiply scattered coherent light: An analytical model for anisotropically scattering media," Phys. Rev. E **66**, (026603) 1-9 (2002).

23. F. A. Marks, H. W. Tomlinson, and G. W. Brooksby, "Comprehensive approach to breast cancer detection using light: photon localization by ultrasound modulation and tissue characterization by spectral discrimination," in *Photon Migration and Imaging in Random Media and Tissue*, B. Chance and R. R. Alfano, eds., Proc. SPIE **1888**, 500-510 (1993).

24. L.-H. Wang, S. L. Jacques, and X. Zhao, "Continuous-wave ultrasonic modulation of scattered laser light to image objects in turbid media," Opt. Lett. **20**, 629-631 (1995).

25. L.-H. Wang and X. Zhao, "Ultrasound-modulated optical tomography of absorbing objects buried in dense tissue-simulating turbid media," Appl. Opt. **36**, 7277-7282 (1997).

26. Kempe, M. Larionov, D. Zaslavsky, and A. Z. Genack, "Acousto-optic tomography with multiple scattered light," J. Opt. Soc. Am. **14**, 1151-1158 (1997).

27. S. Leveque, A. C. Boccara, M. Lebec, and H. Saint-Jalmes, "Ultrasonic tagging of photon paths in scattering media: parallel speckle modulation processing," Opt. Lett. **24**, 181-183 (1999).

28. G. Yao and L.-H. Wang, "Theoretical and experimental studies of ultrasound-modulated optical tomography in biological tissue," Appl. Opt. **39**, 659-664 (2000).

29. J. Li and L.-H. V. Wang, "Methods for parallel-detection-based ultrasound-modulated optical tomography," Appl. Opt. **41**, 2079-2084 (2002).

30. J. Selb, L. Pottier, and A. C. Boccara, "Nonlinear effects in acousto-optic imaging," Opt. Lett. **27**, 918-920 (2002).

31. J. Li, Geng Ku, and L.-H. V. Wang, "Ultrasound-modulated optical tomography of biological tissue using contrast of laser speckles," Appl. Opt. **41**, 6030-6035 (2002).

32. J. Li, S. Sakadžić, G. Ku, and L.-H. V. Wang, "Transmission- and side-detection configurations in ultrasound-modulated optical tomography of thick biological tissues,"Appl. Opt. **42**, 4088-4094 (2003).

33. S. Leveque-Fort, "Three-dimensional acousto-optic imaging in biological tissues with parallel signal processing," Appl. Opt. **40**, 1029-1036 (2000).

34. L.-H. Wang and G. Ku, "Frequency-swept ultrasound-modulated optical tomography of scattering media," Opt. Lett. **23**, 975-977 (1998).

35. G. Yao, S. Jiao, and L.-H. Wang, "Frequency-swept ultrasound-modulated optical tomography in biological tissue by use of parallel detection," Opt. Lett. **25**, 734-736 (2000).

36. B. C. Forget, F. Ramaz, M. Atlan, J. Selb, and A. C. Boccara, "High-contrast fast Fourier transform acouto-optical tomography of phantom tissues with a frequency-chirp modulation of the ultrasound," Appl. Opt. **42**, 1379-1383 (2003).

37. M. Hisaka, T. Sugiura, and S. Kawata, "Optical cross-sectional imaging with pulse ultrasound wave assistance," J. Opt. Soc. Am. A **18**, 1531-1534 (2001).

38. A. Lev and B. G. Sfez, "Pulsed ultrasound-modulated light tomography," Opt. Lett. **28**, 1549-1551 (2003).

39. J. Li and L.-H. V. Wang, "Ultrasound-modulated optical computed tomography of biological tissues," Appl. Phys. Lett. **84**, 1597-1599 (2004).

40. A. Lev, Z. Kotler, and B. G. Sfez, "Ultrasound tagged light imaging in turbid media in a reflectance geometry," Opt. Lett. **25**, 378-380 (2000).

41. A. Lev and B. G. Sfez, "Direct, noninvasive detection of photon density in turbid media," Opt. Lett. **27**, 473-475 (2002).

42. S. Leveque-Fort, J. Selb, L. Pottier, A. C. Boccara, "In situ local tissue characterization and imaging by backscattering acousto-optic imaging,' Opt. Commun. **196**, 127-131 (2001).

43. A. H. Hielscher, J. R. Mourant, and I. J. Bigio, "Influence of particle size and concentration on the diffuse backscattering of polarized light from tissue phantoms and biological cell suspensions," Appl . Opt. **36,** 125–135 (1997).

44. J. F. de Boer, T. E. Milner, M. J. C. van Gemert, and J. S. Nelson, “Two-dimensional birefringence imaging in biological tissue by polarization-sensitive optical coherence tomography,” Opt. Lett. **22**, 934–936 (1997).

45. S. G. Demos and R. R. Alfano, “Optical polarization imaging,” Appl. Opt. **36,** 150–155 (1997).

46. V. Sankaran, K. Schonenberger, J. T. Walsh, Jr., and D. J. Maitland, “Polarization discrimination of coherently propagating light in turbid media,” Appl. Opt. **38,** 4252–4261 (1999).

47. S. L. Jacques, J. R. Roman, and K. Lee, “Imaging superficial tissues with polarized light,” Lasers in Surg. & Med. **26,** 119–129 (2000).

48. V. Sankaran, M. J. Everett, D. J. Maitland, and J. T. Walsh, Jr., “Comparison of polarized-light propagation in biological tissue and phantoms,” Opt. Lett. **24,** 1044–1046 (1999).

49. J. W. Goodman, “Statistics properties of laser speckle patterns,” in *Laser Speckle and Related Phenomenon*, J. C. Dainty ed. (Springer-Verlag, Berlin, 1975), pp. 9–75.

50. A. F. Fercher and P. F. Steeger, “First-order statistics of Stokes parameters in speckle fields,” Opt. Acta **28**, 443–448 (1981).

51. P. F. Steeger and A. F. Fercher, “Experimental investigation of the first-order statistics of Stokes parameters in speckle fields,” Opt. Acta **29**, 1395–1400 (1982).

52. R. Barakat, “The statistical properties of partially polarized light,” Opt. Acta **32**, 295–312 (1985).

53. C. Brosseau, “Statistics of the normalized Stokes parameters for a Gaussian stochastic plane wave field,” Appl. Opt. **34**, 4788–4793.
54. I. Freund, M. Kaveh, R. Berkovits, and M. Rosenbluh, “Universal polarization correlations and microstatistics of optical waves in random media,” Phys. Rev. B **42,** 2613–2616 (1990).
55. I. I. Tarhan and G. H. Watson, “Polarization microstatistics of laser speckle,” Phys. Rev. A **45,** 6013–6018 (1992).
56. P. Elies, B. LeJeune, F. LeRoyBrehonnet, J. Cariou, and J. Lotrian, “Experimental investigation of the speckle polarization for a polished aluminium sample,” J. Phys. D: Appl. Phys. **30,** 29–39 (1997).
57. J. Li, G. Yao, and L.-H. V. Wang, “Degree of polarization in laser speckles from turbid media: Implications in tissue optics,” J. Biomed. Opt. **7**, 307–312 (2002).
58. J. P. Mathieu, *Optics*, Pergamon Press, New York (1975).
59. J. C Dainty, “Introduction,” in *Laser Speckle and Related Phenomenon*, J. C. Dainty ed.. (Springer-Verlag, Berlin, 1975), pp. 1–7.
60. A. E. Ennos, “Speckle interferometry,” in *Laser Speckle and Related Phenomenon*, J. C. Dainty ed.. (Springer-Verlag, Berlin, 1975), pp. 203–253.
61. R. A. Chipman, “Polarimetry,” *Handbook of Optics*, M. Bass, ed.. Optical Society of America, Washington, D. C. (1995).
62. S. Jiao, G. Yao, and L.-H. V. Wang, “Depth-resolved two-dimensional Stokes vectors of backscattered light and Mueller matrices of biological tissue measured by optical coherence tomography,” Appl. Opt. **39**, 6318–6324 (2000).

63. J. Selb, S. Leveque-Fort, L. Pottier, and C. Boccara, “Setup for simultaneous imaging of optical and acoustic contrasts in biological tissues,” in *Biomedical Optoacoustics II*, Alexander A. Oraevsky eds., Proc. SPIE **4256**, 200-207 (2001).
64. C. A. Thompson, K. J. Webb, and A. M. Weiner, “Imaging in scattering media by use of laser speckle,” J. Opt. Soc. Am. **A14**, 2269-2277 (1997).
65. J. D. McKinney, M. A. Webster, K. J. Webb, and A. M. Weiner, “Characterization and imaging in optically scattering media by use of laser speckle and a variable-coherence source,” Opt. Lett. **25**, 4-6 (2000).
66. P. Naulleau, D. Dilworth, E. Leith, and J. Lopez, “Detection of moving objects embedded within scattering media by use of speckle methods,” Opt. Lett. **20**, 498-500 (1995).
67. G. Parry, “Some effects of temporal coherence on the first order statistics of speckle,” Opt. Acta **21**, 763-772 (1974).
68. D. A. Zimnyakov, V. V. Tuchin, and S. R. Utts, “A study of statistical properties of partially developed speckle fields as applied to the diagnostics of structural changes in human skin,” Opt. Spectrosc. **76**, 838-844 (1994).
69. S. L. Jacques and S. J. Kirkpatrick, “Acoustically modulated speckle imaging of biological tissues,” Opt. Lett. **23**, 879-881 (1998).
70. G. Marquez and L.-H. Wang, “White light oblique incidence reflectometer for measuring absorption and reduced scattering spectra of tissue-like turbid media,” Optics Express **1**, 454-460 (1997).

71. American National Standards Institute, *American National Standard for the Safe Use of Lasers in Heath Care Facilities. Standard Z136.1-2000.* (ANSI, Inc., New York, NY, 2000).

72. G. Marquez, L.-H. V. Wang, S. P. Lin, J. A. Schwartz, and S. L. Thomsen**,** "Anisotropy in the absorption and scattering spectra of chicken breast tissue," Appl. Opt. **37**, 798-804 (1998).

73. Y. Watanabe, T. Yuasa, T. Akatsuka, B. Devaraj, and H. Inaba, "Enhacement of laser CT image contrast by correction of artifacts due to surface effects," Opt. Express **3**, 104-110 (1998).

74. R. G. Kelly, K. J. Jordan, and J. J. Battista, "Optical CT reconstruction of 3D dose distributions using the ferrous-benzoic-xylenol (FBX) gel dosimeter," Med. Phys. **25**, 1741-1750 (1998).

75. K. Chen, L. T. Perelman, Q. Zhang, R. R. Dasari, and M. S. Feld, "Optical computed tomography in a turbid medium using early arriving photons," J. Biomed. Opt. **5**, 144-154 (2000).

VITA

CONTACT

Name: Jun Li
Address: 135 Longxiang Street, Apt. 11341, Kunming, Yunnan 650031, P. R. China
E-mail: tamujunli@yahoo.com

EDUCATION

Ph.D., Biomedical Engineering 08/2004
Texas A&M University, College Station, Texas, USA

Ph.D., Physical Electronics and Optoelectronics 07/1997
Huazhong University of Science and Technology, Wuhan, Hubei, P. R. China

M. Eng., Physical Electronics and Optoelectronics 07/1993
Huazhong University of Science and Technology, Wuhan, Hubei, P. R. China

B. Eng., Optical Engineering 07/1990
Huazhong University of Science and Technology, Wuhan, Hubei, P. R. China